Rupture to the trench? Frictional properties and fracture energy of incoming sediments at the Cascadia subduction zone

C. E. Seyler[1,*], J. D. Kirkpatrick[1], H. M. Savage[2], T. Hirose[3], and D. R. Faulkner[4]

[1] Department of Earth and Planetary Sciences, McGill University, Montréal, QC, Canada

[2] Department of Earth and Planetary Sciences, University of California, Santa Cruz, CA, USA

[3] Kochi Institute for Core Sample Research, Japan Agency for Marine-Earth Science and Technology, Kochi, Nankoku, Japan

[4] School of Environmental Sciences, University of Liverpool, Liverpool, UK

* *Corresponding author*: Caroline Seyler (caroline.seyler@mail.mcgill.ca)

Abstract

The mechanical properties of sediment inputs to subduction zones are important for understanding rupture propagation through the accretionary prism during megathrust earthquakes. Clay minerals strongly influence the frictional behavior of fault gouges, and the clay content of subduction input materials varies through a stratigraphic section as well as for subduction margins globally. To establish the frictional properties of the shallow Cascadia subduction zone and place the results in a global context, we conducted high velocity rotary shear experiments on ODP core samples retrieved from Cascadia input sediments (35-45% clay) and a suite of individual clay species. We compared our results to a compilation of published high velocity experiments conducted on samples of wet gouge, dry gouge, and intact rock. For each sample type, three trends were

identified with increasing normal stress: 1) the stress drop ($\tau_p - \tau_{ss}$) increases linearly, 2) the characteristic thermal weakening distance (D_{th}) decreases as a power law function except for wet clay-rich gouges, and 3) the fracture energy (W_b) shows no dependence. However, fracture energy does vary with sample type. Clay-rich gouges under wet conditions have the lowest fracture energy, and fracture energy for both dry and wet gouges is at least an order of magnitude lower than estimates from intact rocks. Therefore when clay-rich lithologies are present, they may minimize spatial variations in frictional behavior, allowing earthquakes to propagate to the trench. For Cascadia input sediments, there is little variation in the fracture energy between lithologies, but the fracture energy of Cascadia sediments is around an order of magnitude higher than input sediments from other subduction margins. The high fracture energy of Cascadia sediments relative to other subduction margins may inhibit large amounts of shallow earthquake slip and dynamic overshoot.

1 Introduction

The 2004 Sumatra (M_w 9.1-9.3) and 2011 Tohoku-Oki (M_w 9.1) earthquakes emphasized that damaging tsunamis are promoted by large amounts of shallow coseismic slip during megathrust earthquakes (Bletery et al., 2016; Lay, 2018). Shallow slip requires rupture to propagate through the accreted sediments updip of the seismogenic zone. Clay-rich pelagic and hemipelagic sediments host the décollement zone at many subduction margins, such as Barbados, Costa Rica, the Japan Trench, and northern Cascadia (Han et al., 2017; Ikari et al., 2018; Moore et al., 2015; Vrolijk, 1990). The frictional properties of clay-rich sediments, particularly at high velocity, are therefore a primary control on earthquake propagation near the trench (Faulkner et al., 2011; Ikari and Kopf, 2017). For example, slip during the 2011 Tohoku-Oki earthquake most likely localized into clay-rich sediments (Chester et al., 2013; Kirkpatrick et al., 2015; Rabinowitz et al., 2020). Existing laboratory rock friction measurements indicate that at fast (~m/s) sliding velocities, clay-rich sediments weaken rapidly with slip and are characterized by low fracture energy (e.g. Faulkner et al., 2011; Sawai et al., 2014; Ujiie et al., 2013).

Earthquake fracture energy has been defined as the work done during dynamic weakening (Palmer and Rice, 1973) that includes an unknown partitioning between energy dissipated during fracturing and/or plastic deformation and heat dissipation during frictional sliding (Tinti et al., 2005). Fracture energy dictates the energy required for rupture propagation and the local accelerations on a fault during slip, and low fracture energy may encourage propagation to the trench during large megathrust earthquakes. The slip-weakening model describes the shear stress at a point on a fault during an earthquake as it evolves with slip. Shear stress increases to a peak, then decays to a steady state shear stress over a characteristic amount of slip, the slip weakening distance (Ida, 1972; Palmer and Rice, 1973). In this model, fracture energy (G) is defined as the work performed as shear stress decays linearly over the slip weakening distance and is written as

$$G = \frac{1}{2}(\tau_p - \tau_{ss})D_c \tag{1}$$

where τ_p is the peak shear stress prior to the onset of weakening, τ_{ss} is the steady state shear stress, and D_c is the slip weakening distance. A general expression for fracture energy that does not rely on a particular shear stress evolution was defined by Abercrombie and Rice (2005) as

$$G(\delta) = \int_0^{\delta} [\tau(\delta') - \tau(\delta)]d\delta' \tag{2}$$

where τ is shear stress, δ' is slip and δ is final slip. On the shallow portions of subduction zones, where the lithostatic load is low, incremental depth changes result in relatively significant changes in normal stress when compared to the total lithostatic load. Thus, the energy budget for shallow earthquake slip may be sensitive to depth depending on how fracture energy, frictional heating, and radiated energy change with normal stress.

Seismological estimates of fracture energy (hereafter G') are derived from seismic waveforms rather than direct measurements of shear stress on a fault. Estimates of seismological fracture energy indicate that total fracture energy for an earthquake scales as a power law function of the total slip (Abercrombie and Rice, 2005; Nielsen et al., 2016). Tsunami earthquakes, which occur on the shallow parts of some subduction zones, deviate from this general trend. These earthquakes can have significant amounts of slip but lack high frequency radiated energy, instead dissipating a larger fraction of their total energy as fracture energy relative to ordinary earthquakes (Kanamori, 1972; Venkataraman and Kanamori, 2004). The causes of tsunami earthquakes remain unclear, but the significant differences in the dynamics of tsunami earthquakes suggest fracture energy of sediments in the accretionary prism has important implications for rupture propagation.

At the Cascadia subduction zone, little is currently known about the frictional behavior of the shallow part of the megathrust. Paleoseismic records indicate a history of M_w 8 and M_w 9 earthquakes that ruptured all or significant portions of the subduction zone, suggesting rupture to the trench may be a common feature of large events at this margin (Goldfinger et al., 2012), though there are few small to moderate earthquakes to define the seismogenic zone limits. Geodetic measurements and heat flow data that indicate the thermally defined updip limit to the seismogenic zone is near the trench (Li et al., 2018; Oleskevich et al., 1999). At low velocity, sediments from the input section along the southern Cascadia margin have relatively high coefficients of friction of 0.4-0.5 (Ikari and Kopf, 2017), which increases the potential for stored elastic strain energy at shallow depth. However, the high velocity frictional behavior of sediments from Cascadia has not been measured, so the implications for rupture propagation are not fully defined. In this study, we conducted high velocity friction experiments on drill core samples of sediments from the Juan de Fuca plate that are the input to the Cascadia subduction zone to explore the effects of clay content and normal stress on their frictional behavior. We also measured the frictional behavior of individual clay species and compare our results to previously reported studies on gouges from other plate boundary faults to investigate whether Cascadia may be more prone to rupture to the trench than other margins.

2 Materials and Methods

2.1 Cascadia sample characterization

Core samples were obtained from two Ocean Drilling Program (ODP) sites near the Cascadia subduction zone: Site 888 of Leg 146 (Carson et al., 1995) and Site 1027 of Leg 168 (Fisher et al., 2000) (Fig. 1a). Though neither site sampled the complete input stratigraphic section immediately seaward of the trench, when combined, cores from these sites capture the lithologic variation expected throughout the input stratigraphic section overlying the basalt basement. Three similar stratigraphic units are present at both sites (Fig. 1b): interbedded sand and silt turbidites (Subunit 1A at Site 1027/Unit II at Site 888), interbedded silt turbidites and hemipelagic mud (Subunit 1B at Site 1027/Unit III at Site 888), and hemipelagic mudstone (Unit II at Site 1027). An additional unit of indurated mudstone, basalt talus, and diabase sills is present at Site 1027 (Unit III) (Carson et al., 1995; Fisher et al., 2000). At Site 1027, where the mineralogy has been previously characterized, clay content varies by lithology, and includes smectite, illite, chlorite, and kaolinite

(Fisher et al., 2000). When the stratigraphy documented at Site 1027 is projected beneath the hole at Site 888, Site 1027 represents a relatively deep section of the stratigraphy near the trench. The hemipelagic mudstone present at Site 1027 represents the material most likely to be present at the décollement based on interpretation of seismic reflection data (Fig. 1c).

Three samples were selected for high velocity friction experiments to represent the input section to the Cascadia subduction zone: 1) core sample 146-888B-62X-2 (Leg-Site-hole-core-section) is a hemipelagic mudstone recovered from an approximate depth of 534.17 m beneath seafloor (mbsf), 2) core sample 168-1027B-03H-3 is from a layer with sand-sized grains within the interbedded turbidites (17.45 mbsf), and 3) core sample 168-1027B-53X-2 is a hemipelagic mudstone (493.55 mbsf). Sample composition was determined from X-ray diffraction and Rietveld refinement (see supplement for methods) and shows all three samples contain the same clay species, but there are variations in the clay content between lithologies (Table S1; Fig. S1). The Site 1027 sandstone contains 35% clay-sized fraction with the remainder split between quartz (30%) and feldspar (35%), while the Site 888 and 1027 mudstones both contain 45% clay-sized fraction, 20% quartz, and 35% feldspar. The uncertainty of these percentages is on the order of 5%. Smectite (montmorillonite), illite, and chlorite were identified in the clay fraction of all three samples (Fig. S2), but the lack of crystallinity prohibits a quantitative analysis of the proportions of phases in the clay fraction.

2.2 Experimental procedure for tests on Cascadia samples

Friction experiments were conducted in the servo-controlled low to high velocity rotary shear apparatus (Fig. 2) at Kochi/JAMSTEC (Tanikawa et al., 2012). High velocity tests were conducted on synthetic gouges prepared from the three ODP core samples at 2, 5, and 8 MPa normal stress. Samples were dried in a 60 ˚C oven overnight before being disaggregated in a mortar and pestle and sieved to <250 μm. For each experiment, 15 g of sample powder was combined with 2 ml of distilled water to produce wet synthetic gouges. These gouges were placed between two annular steel sample holders with inner and outer radii of 15 and 30 mm, respectively, and then surrounded by an inner and outer Teflon jacket. The mechanical contribution of the Teflon was tested by conducting an experiment with no applied normal load and a gap between the sample holders. The shear stress contributed by the Teflon jacket was near zero (see supplement and Fig. S3), and we did not correct for the negligible mechanical influence of the Teflon jacket or o-ring. Gouge samples were pre-compacted by a combination of three manual rotations at <1 MPa normal stress followed by a 40-minute hold at the normal stress condition of the experiment, producing an initial gouge zone thickness of approximately 2-3 mm. All tests were conducted at room temperature (25.5 ˚C) and humidity (31-34%).

For the annular sample holder, linear slip velocity varies from the inner to the outer diameter, so an equivalent slip velocity may be defined for analysis. Assuming shear stress is not dependent on velocity, the total frictional work on a fault is $W = \tau v_{eq} A$, where A is the cross-sectional area and v_{eq} is the equivalent slip velocity. The v_{eq} is then defined as

$$v_{eq} = \frac{4\pi R(r_1^2 + r_1 r_2 + r_2^2)}{3(r_1^2 + r_2^2)} \quad (3)$$

where R is the revolution rate of the motor and r_1 = 15 mm and r_2 = 30 mm are the inner and outer radii of the sample holder, respectively (Hirose and Shimamoto, 2005). Samples were first deformed at a nominal v_{eq} of 0.5 to 100 μm/s over a total displacement of approximately 100 mm to establish a deformation fabric. Then, samples were deformed at a nominal v_{eq} of 500 μm/s for

0.2 rotations, then accelerated at a rate of 0.2 m/s^2 to the target nominal v_{eq} of 1 m/s for 35 rotations for a constant total displacement of 10.5 m (Fig. S4a). At the end of the experiment, v_{eq} was decelerated at the same rate to 500 μm/s before terminating the experiment.

2.3 Experimental procedure for tests on individual clay species

High velocity experiments were also conducted on five samples of commercially available clay-rich materials. The principal clay components for these powders are illite, pyrophyllite, montmorillonite, sericite and talc. The purity, accessory components, and the sources for each gouge type are listed in Table S2. All mineralogical components were identified by X-ray diffraction using Rietveld refinement. The uncertainty of the percentages is on the order of 5%.

Individual clay species experiments were conducted on a high velocity rotary shear apparatus at Kochi/JAMSTEC (for details see supplement and Tsutsumi and Shimamoto (1997)) at normal loads ranging from 0.7 to 3.25 MPa. A layer of gouge was produced from 1 g of the sample material placed between two solid gabbro slider blocks of a nominal 25 mm diameter. The surfaces of the slider blocks in contact with the gouge were prepared using SiC #80 powder. The layers of gouge were contained by a Teflon sleeve that was manufactured to fit tightly on the slider blocks, the same arrangement used by Mizoguchi et al. (2007). The mechanical contribution of the Teflon was tested by running an experiment with no applied normal load. The shear stress of the Teflon was below the measured shear stresses of the synthetic gouges at their lowest level (see supplement and Fig. S3), and we have not corrected the data for the negligible mechanical influence of the Teflon sleeve. Prior to running the tests at high velocity, the normal load was applied to the sample and the sliding blocks were rotated relative to one another to pre-compact the gouge. The precompaction resulted in a gouge layer of approximately 1 mm thickness and porosity of ~50%. For the tests conducted under wet conditions, 0.5 ml of de-ionized water was added to the gouge prior to assembly.

All tests were run at a nominal v_{eq} of 1.3 m/s with an initial acceleration ramp of ~10 m/s^2 (Fig. S4b). The motor was first accelerated to the desired speed, then engaged with the sample via the magnetic clutch assembly. This accelerated the rotating side of the sample assembly to 1.3 m/s over a slip distance of around 10 cm. When the desired slip distance for an experiment was achieved, the motor was switched off and the sample decelerated due to friction.

2.4 Estimation of fracture energy from high velocity experiments

Fracture energy can be estimated from high velocity friction experiments as proportional to the product of shear stress and slip weakening distance. We estimated the breakdown work (W_b) and the thermal weakening distance (D_{th}) directly from the shear stress evolution recorded on the experimental fault (Fig. 2c). W_b is the work associated with dynamic weakening from peak (τ_p) to steady state shear stress (τ_{ss}), equivalent to fracture energy (G), and is considered comparable to seismological estimates of fracture energy (G') (Tinti et al., 2005). W_b is dependent on the breakdown stress drop ($\tau_p - \tau_{ss}$) and the thermal weakening distance (D_{th}), a characteristic slip weakening distance. D_{th} represents the amount of slip necessary for the shear stress to be reduced to 1/e of $\tau_p - \tau_{ss}$. Previous definitions for the slip weakening distance (D_c) defined the characteristic distance based on a 95% reduction of the initial $\tau_p - \tau_{ss}$ value (Mizoguchi et al., 2007). We prefer D_{th} because it captures the significant initial phase of weakening triggered by thermally induced weakening mechanisms (Di Toro et al., 2011). To estimate these parameters, the shear stress curve from each experiment was fit with a least-squares approach to the following exponential decay equation as defined by Di Toro et al. (2011)

$$\tau = \tau_{ss} + \left(\tau_p - \tau_{ss}\right) e^{-\frac{\delta}{D_{th}}} \tag{4}$$

where τ_{ss} is the steady state shear stress (MPa), τ_p is the peak shear stress (MPa), D_{th} is the thermal weakening distance (m), and δ is the slip accumulated after the peak shear stress (m). W_b was then estimated by integrating under the modeled shear stress curve from the slip at τ_p to D_{th}

$$W_b = \int_0^{D_{th}} \left(\tau_p - \tau_{ss}\right) e^{-\frac{\delta}{D_{th}}} \, d\delta \tag{5}$$

for each experiment.

3 Experimental results

3.1 Cascadia core samples

All of the high velocity experiments (Fig. 3) exhibited a similar stress evolution to previously published results for gouges (e.g. Mizoguchi et al., 2007). Following the run-in phase, v_{eq} was accelerated from 500 µm/s to 1 m/s, which resulted in an increase in shear stress from the initial (τ_0) up to a peak (τ_p), followed by a decay to a lower steady state value (τ_{ss}). τ_0 and τ_p are higher for the Site 1027 sandstone than the Site 888 and 1027 mudstones, however nearly all experiments across the range of normal stresses tested have τ_{ss} around 1-2 MPa (Table 1). Experiments conducted on the Site 1027 sandstone at all normal stresses and the Site 888 and 1027 mudstones at a normal stress of 8 MPa saw an increase of shear stress at the end of the experiment during deceleration, possibly related to dynamic healing or a loss of pore fluids.

For all three samples, τ_p scales linearly with normal stress and the friction coefficients at peak stress (μ_p) are 0.67 for the 1027 sandstone and 0.40-0.46 for the mudstones (Fig. 4a). These friction coefficients are higher than those observed at slower slip velocities (Fig. S3) because of the increase in shear stress associated with increasing slip velocity (e.g. Cocco and Bizzarri, 2002). τ_{ss} did not change significantly with normal stress and the friction coefficients at steady state (μ_{ss}) are 0.04-0.06 for all samples (Fig. 4a). This small variation in the steady state behavior between the samples indicates viscous-type deformation in each experiment, similar to what was observed at the Japan Trench Fast Drilling Project (JFAST) by Ujiie et al. (2013). As a consequence of the minimal change in τ_{ss} with normal stress, $\tau_p - \tau_{ss}$ increases linearly with normal stress and is larger for the sandstone sample (Fig. 4a). However, the thermal weakening distance (D_{th}) decreases with normal stress and is larger for the mudstone samples (Fig. 4b; Table 1). As a result of the opposite dependence on normal stress for these two parameters, there is only a small variation in the breakdown work (W_b) (Fig. 4c; Table 1), which varies by <2 MJ/m^2 for each sample.

3.2 Individual clay species

Experiments conducted on samples of individual clay species followed the same overall trends in mechanical behavior as the Cascadia samples and the frictional behavior of each clay species was generally similar (also see Faulkner et al. (2011)). Under dry conditions, τ_p and τ_{ss} increase linearly with normal stress for each clay species (Fig. 5a-c). Under wet conditions, τ_p increases linearly, but τ_{ss} does not significantly increase, again suggesting viscous-type deformation (Fig. 5d-f). In both dry and wet experiments, the friction coefficients at peak and steady state are highest for illite and pyrophyllite and lowest for talc and montmorillonite (Fig. S6). For all clay species, $\tau_p - \tau_{ss}$ is smaller for the wet experiments. D_{th} decreases with normal stress under dry conditions for each clay species, but there is no apparent trend under wet conditions with the exception of montmorillonite. Instead, under wet conditions D_{th} ranges over approximately three orders of magnitude. Generally, montmorillonite has the lowest breakdown work (W_b) while pyrophyllite has the highest. W_b shows no dependence on normal stress for most clay species, but there is a possible weak dependence for sericite and montmorillonite under dry conditions and illite under wet conditions. Overall, W_b varies in magnitude between different clay species by up to three orders of magnitude and does not appear to vary systematically with normal stress.

4 Discussion

4.1 Data compilation of high velocity friction experiments

The experiments on Cascadia core samples demonstrate that the breakdown stress drop ($\tau_p - \tau_{ss}$) and thermal weakening distance (D_{th}) are dependent on normal stress, but the breakdown work (W_b) shows little variation. Additionally, of the three Cascadia samples, the Site 1027 sandstone has the highest τ_p and τ_{ss}, suggesting clay content plays a role in determining the overall frictional behavior. Individual clay species deformed under wet conditions have extremely low values for D_{th} and W_b with no clear dependence on normal stress. Together, the two sets of experiments suggest W_b may be independent of normal stress, and that clay content and the presence of water may be significant controls on the overall frictional behavior and fracture energy of a rock, as noted previously (e.g. Faulkner et al., 2011; Ikari et al., 2009).

To further explore the effect of normal stress and understand the role of clay content in the frictional behavior of fault rocks at high slip rates, we compiled laboratory estimates of peak and steady state shear stress, slip weakening distance, and fracture energy from 233 experiments conducted on 5 different machines reported in 20 previous studies (Fig. 6; Table S3). The compiled data were separated into three categories: 1) gouges deformed under wet conditions, 2) gouges deformed under dry conditions, and 3) intact rocks deformed under dry conditions. Previously reported slip weakening distance and fracture energy values were converted to D_{th} and W_b (see supplement Section S3 and Fig. S5 for details).

The linear scaling of $\tau_p - \tau_{ss}$ with normal stress is a common feature of all datasets (Fig 6a). Most of the compiled gouge experiments were conducted at a normal stress of 5 MPa or less. The data at these low normal stresses show that the constant of proportionality between $\tau_p - \tau_{ss}$ and normal stress decreases with increasing clay content for both wet and dry gouges. Notably, the wet gouges generally have lower slopes than the dry gouges. Intact rocks have a similar range for constants of proportionality as the dry gouges. These results show the $\tau_p - \tau_{ss}$ scaling is a material property dictated by τ_p scaling with normal stress (μ_p) and is not significantly modified by smaller increases in τ_{ss} with increasing normal stress.

D_{th} decreases as a power law function of normal stress for dry gouges and intact rocks, but there is no clear variation with clay content (Fig. 6b). The power law exponents (i.e. the slopes) appear similar for dry gouges and intact rocks. The wet gouges do not exhibit any clear dependence of D_{th} on normal stress, with values ranging over three orders of magnitude. Within wet gouges, D_{th} behaves systematically for some individual clay species, such as montmorillonite, while others show no trend with normal stress (Fig. 5). Lack of a systematic dependence on normal stress is representative of most wet gouges (e.g. Sawai et al., 2014) and there is also no clear relationship between D_{th} and clay content.

W_b exhibits no scaling with normal stress for any of the categories (Fig. 6c). The absence of a relationship between fracture energy and normal stress has been reported previously (Nielsen et al., 2016). Within the wet gouges, illite demonstrates a possible weak dependence on normal stress (Fig. 5), but most datasets under wet or dry conditions show no such dependence, including datasets compiled from the literature as well as those from this study (e.g. Cascadia results in Fig. 4; other phases in Fig. 5; French et al., 2014; Mizoguchi et al., 2007; Sawai et al., 2014). W_b values for dry gouges overlap with the highest W_b values for wet gouges, but the smallest W_b values for wet gouges are three orders of magnitude lower than the other two categories. Neither wet nor dry gouges show any clear trends with clay content, but the magnitude of W_b does vary with clay species (Fig. 5).

Finally, there is a strong dependence between $\tau_p - \tau_{ss}$ and D_{th} for dry gouges and intact rocks, but there is no such dependence for wet gouges (Fig. 6d). This represents a fundamentally different behavior for wet and dry conditions. A correlation between $\tau_p - \tau_{ss}$ and D_{th} is expected for dry conditions where both of these two parameters were observed to vary with normal stress. As effective normal stress was not measured in the slip zone during the experiments, a trend with normal stress for wet gouges might be hidden in the normal stress uncertainty. However, the absence of a correlation between D_{th} and $\tau_p - \tau_{ss}$ suggests the lack of scaling with applied normal stress for wet gouges is robust despite not measuring pore fluid pressure or effective normal stress during experiments conducted under wet conditions.

The compiled data suggest that W_b is independent of normal stress, despite $\tau_p - \tau_{ss}$ and D_{th} having strong dependencies on normal stress for intact rocks and dry gouges. We developed an expression for W_b derived from the expressions for $\tau_p - \tau_{ss}$ and D_{th} to validate the lack of scaling for W_b. We fit the observed linear relationship between normal stress and $\tau_p - \tau_{ss}$ following the equation

$$\tau_p - \tau_{ss} = a_1 \sigma_n \quad (6)$$

where a_1 is a coefficient and σ_n is normal stress. We also fit the observed power law relationship between normal stress and D_{th} following the equation

$$D_{th} = a_2 \sigma_n^{-b} \quad (7)$$

where a_2 is a coefficient and b is the power law exponent (Di Toro et al., 2011). Using equations 6 and 7, the equation for estimating W_b (Eq. 1; Di Toro et al., 2011) can be re-written as

$$W_b = \frac{1}{2} a_1 a_2 \sigma_n^{1-b} \quad (8)$$

with b expected to be near 1 to cancel the dependence on normal stress. For each dataset or subset, we used a nonlinear least-squares fit and report a 95% confidence interval for equations 6 and 7 (Table 2). The wet and dry gouges were separated into three groups by clay content due to the strong influence of clay on the friction coefficient and therefore the magnitude of $\tau_p - \tau_{ss}$, resulting in different values for a_1. The wet gouge categories are too scattered for any reasonable model fit for D_{th} or W_b. Most of these fits are associated with large uncertainty due to the spread of data in each category, but all resulting exponents for the relationship between normal stress and W_b are near zero, reflecting no dependence on normal stress due to the tradeoff between increasing $\tau_p - \tau_{ss}$ and decreasing D_{th}. Projecting the results for dry gouges and intact rocks to seismogenic depths of ~10 km by approximating the normal stress as lithostatic stress suggests $\tau_p - \tau_{ss}$ would range from 10s of MPa near the surface to 100s of MPa at seismogenic depths, D_{th} would vary from meters near the surface to centimeters or millimeters at seismogenic depths, yet W_b would not vary significantly.

The majority of the compiled experiments were conducted on the high velocity rotary shear machine at Kochi/JAMSTEC (“HVR”), but some experiments were conducted on other machines at Kochi/JAMSTEC, Kyoto University, Hiroshima University, and INGV in Italy. Significant differences in boundary conditions between rotary shear machines, such as sample dimension and thermal conductivity and permeability of sample holders, may lead to some variation in the experimental results (Savage et al., 2018; Yao et al., 2016). Additionally, differences in the acceleration path will increase τ_p and decrease D_{th}, but not affect τ_{ss} (Sone and Shimamoto, 2009). These combined acceleration effects may cancel each other and produce a small effect on W_b. Though we have not controlled for these differences, there are still clear trends that emerge from the compilation, suggesting these trends are robust despite the data being sourced from various machines at multiple labs.

4.2 Comparison of gouges and intact rocks

The compiled data indicate that, in general, dynamic weakening during seismic slip is influenced by the clay content, the presence of water, and the material state (i.e. gouge or intact rock). Clay content controls the initial strengthening (τ_p) for gouge samples (Fig. 6a), which is expressed by a_1 in Eq. 8 and decreases with increasing clay fraction (Table 2). Results for intact rocks vary with rock type (e.g. a_1 = 0.57 for calcite, a_1 = 0.45 for peridotite), but wet clay-rich gouges have the smallest values of a_1 (0.19). The rate of weakening (D_{th}) does not systematically vary with clay content for wet or dry gouges (Fig. 6b). The length of D_{th} appears to depend more on the presence of water and the material state of the sample than clay content (e.g. a_2 for intact rocks is an order of magnitude greater than dry gouges, but we found no clear variation of a_2 with clay content within the dry gouges). These characteristics control the porosity, permeability, and thermal diffusivity of the experimental fault, which dictate the pore fluid pressure in the sample (Faulkner et al., 2011; Rice, 2006; Yao et al., 2016). For example, the very small values of D_{th} for wet gouges imply the reduced permeability of wet, particularly clay-bearing, gouges promotes rapid weakening due to the efficacy of thermal pressurization as a weakening mechanism (e.g. Ujiie and Tsutsumi, 2010). Additionally, differences between gouges and intact rocks may also be due to the ability of granular materials to facilitate weakening via non-thermal effects (e.g. shear-enhanced compaction leading to pore pressurization or rolling of grains) (Aretusini et al., 2019; Reches and Lockner, 2010).

Breakdown work (W_b) is dependent on τ_p, τ_{ss}, and D_{th} and thus also influenced by the material properties of the sample and the experimental fault system. These influences manifest as the notable difference in the magnitudes of W_b for each of the three categories (Fig. 6c). W_b for wet gouges ranges two orders of magnitude lower than the range for dry gouges, and W_b for most intact rocks ranges an order of magnitude higher than dry gouges. Differences in W_b are a measure of the efficiency of the weakening mechanism, again suggesting that thermal pressurization (invoked for wet gouges) is more efficient at reaching the necessary temperature for weakening (~150 °C for thermal pressurization) (French et al., 2014; Kitajima et al., 2010) than the mechanisms for dry gouges or intact rocks (e.g. powder lubrication and flash heating) (Di Toro et al., 2011). Overall, the effects of water and material state outweigh clay content in determining D_{th}, but clay content still influences W_b.

4.3 Comparison of laboratory and seismological estimates of fracture energy

Seismological fracture energy (G') is a measure of the energy per unit area for the propagation of the rupture tip and is estimated from earthquake source spectra and the earthquake energy budget (Abercrombie and Rice, 2005). The velocity step from the run-in stage to 1 m/s during the experiments may not be a good representation of the transition from pre-rupture to sliding at a rupture tip for a variety of reasons. However, the magnitudes of lab estimates overlap with seismological estimates of G' (Nielsen et al., 2016; Selvadurai, 2019 and references therein). Though the lab does not directly replicate an earthquake, many of the energy sinks associated with breakdown work during both natural and experimental events are the same (e.g. frictional resistance, comminution, melting, heating of pore fluid, and heat dissipation), suggesting that the lab and seismological estimates are comparable.

The experimental data we compiled exhibits a scaling between W_b and D_{th} that is strikingly similar to the positive scaling between seismological estimates of fracture energy and earthquake size (total slip during the earthquake) (Fig. 7) (Abercrombie and Rice, 2005; Viesca and Garagash, 2015). A similar relationship between fracture energy and earthquake size has also been reproduced in the lab by calculating fracture energy for increments of accumulating slip rather than at D_{th} (Nielsen et al., 2016). Viesca and Garagash (2015) estimated fracture energy based on two definitions: 1) for crack-like ruptures, fracture energy is defined as $G' = \left(\frac{\Delta\tau}{2} - \tau_a\right)\delta$ where $\Delta\tau$ is the static stress drop, τ_a is the apparent stress, and δ is slip, and 2) for pulse-like ruptures, fracture energy is defined as $G^{\max} = G' + \tau_f\delta$ where τ_f is the final fault strength and δ is slip. W_b for wet and dry clay gouges overlap with G' estimates for large earthquakes at subduction zones and major crustal fault zones. Despite the heterogeneity over a rupture area and the importance of acceleration for determining seismological estimates of fracture energy (Tinti et al., 2005), any variation in the acceleration ramp for experiments and natural earthquakes does not overshadow the scaling relationships. In our data, W_b is based on the dynamic stress drop measured at steady state so there is no over- or undershoot. In other words, W_b does not increase further with slip once weakening is complete. The similarity in the experimental and seismological values that arises when D_{th} is equated with total slip therefore supports the idea that ruptures are crack-like on average and may be well explained by a simple slip-weakening model. This also indicates that D_{th} scales with total slip, such that larger earthquakes have larger W_b values on average. The distinction between crack-like vs. pulse-like behavior depends on the background stress level and slip zone thickness, and the agreement between experimental and seismic data supporting crack-like behavior indicates these earthquakes had either high background stress levels or thin slip zones resulting from rapid localization (Noda et al., 2009).

4.4 Implications for the Cascadia subduction zone and other natural faults

The possibility of rupture to the trench at the Cascadia subduction zone depends on the degree of locking at the margin as well as the frictional behavior of the sediments hosting the décollement. The upper limit of the seismogenic zone is thought to extend to the trench based on elevated temperatures at the deformation front exceeding the 100 °C smectite-illite transition (Oleskevich et al., 1999). Locking to the trench is supported by current geodetic fault locking models (Li et al., 2018) and a lack of earthquake epicenters or slow earthquake activity near the trench in northern Cascadia (McGuire et al., 2018; Obana et al., 2015). Offshore of Vancouver Island and Washington state, the décollement is located just above the oceanic basement (Fig. 1; Carson et al., 1995; Han et al., 2017), suggesting that the décollement is likely hosted in hemipelagic mudstones near the base of the thick package of incoming sediments. Friction coefficients of 0.36 and 0.41 (based on pre-acceleration v_e of 500 μm/s, see Fig. S3) for the core samples of hemipelagic mudstones in this study are consistent with previous studies that characterize northern Cascadia as a relatively mechanically strong subduction zone (Cubas et al., 2016; Han et al., 2017). The compiled experimental data show that the fracture energy of the Cascadia input samples under wet conditions is relatively high compared to that of samples representative of other subduction margins such as the Japan Trench and Costa Rica (Fig. 8), likely because the Cascadia samples are relatively clay poor. A lithologic control on subduction zone behavior has been proposed by previous workers (Moore et al., 2015).

Using our measurements from Cascadia samples and the compiled data, we are able to compare the frictional behavior of a diverse set of subduction zone sediments and other fault rocks in detail. Breakdown work (W_b), which is a primary control on rupture dynamics, varies by two orders of magnitude between major plate boundary faults, and by around one order of magnitude for subduction margins (Fig. 8). Clay-rich pelagic rocks have low W_b (e.g. samples retrieved from the Japan Trench; Sawai et al., 2014; Ujiie et al., 2013), whereas clay-poor mudstones dominated by terrigenous input have moderate W_b (e.g. Cascadia and the Nankai Trough; this study; Ujiie and Tsutsumi, 2010). However, there are exceptions to the relationship between clay content and W_b that suggest this relationship is not systematic, such as the moderate W_b of smectite-rich SAFOD fault gouge (Fig. 8). Although paleoseismic records for Cascadia document tsunamis caused by megathrust earthquakes in the past, the moderate W_b of the Cascadia core samples (0.1 to 2 MJ/m^2) compared to other subduction zones may suggest that Cascadia is less susceptible to large amounts of shallow slip and dynamic overshoot. Alternatively, as the Cascadia megathrust is thought to be late in the seismic cycle (Wang et al., 2012), our results raise the possibility that the high frictional strength of the Cascadia core samples, and therefore likely the décollement, may result in higher resolved shear stress on the interface prior to rupture, enhancing the potential for ruptures to propagate to the trench. Additionally, any lithological control on rupture propagation at Cascadia will be limited due to both the lack of variability in the incoming sediment composition and the lack of variability in the frictional behavior between the hemipelagic mudstones and the sandstone samples.

Tsunami earthquakes rupture slowly beneath the shallow part of accretionary prisms at some margins and are characterized by low radiation efficiencies, $\eta_R < 0.25$ ($\eta_R = \frac{E_R}{E_R+G'}$, where E_R is the radiated energy and G' is the seismologically observed fracture energy), relative to ordinary earthquakes (Kanamori, 1972; Venkataraman and Kanamori, 2004). Low radiation efficiency requires an earthquake to dissipate more energy during fault propagation (i.e. W_b) relative to the energy radiated as seismic waves. The compiled results are relevant to tsunami earthquakes because they rupture the shallow portions of subduction zones, where the plate boundary fault zone may contain similar materials to samples from input stratigraphic sections. Although we are not able to evaluate η_R in the experiments because E_R is not measured (and we lack τ_0 for many experiments), in general, high W_b (as a proxy for G') materials may experience tsunami-type events, but low W_b materials would not. As subduction décollements are likely fluid-saturated, Figure 6 suggests that the primary characteristic that might explain tsunami earthquake slip is how well-drained the fault zone is (Ma, 2012), rather than lithology or clay content. If wet gouges predominate in subduction décollements, W_b dissipated on-fault is unlikely to be large, suggesting off-fault damage is also important. Cascadia input materials that contain relatively less clay and exhibit moderately large W_b may therefore be good candidates for hosting tsunami-type events.

5 Conclusions

High velocity rotary shear experiments on input sediments from Cascadia, individual clay species, and experiments on other gouges and intact rocks compiled from the literature have shown that:

1. Mudstones and sandstone from the input sediments at Cascadia are relatively strong (μ_p = 0.40-0.46 and μ_p = 0.67, respectively) and have similar breakdown work values (0.1-2 MJ/m^2) over a range of normal stresses
2. For all sample types, breakdown stress drop increases linearly with normal stress and thermal weakening distance decreases according to a power law dependence on normal stress
3. For all sample types, breakdown work is independent of normal stress due to a tradeoff between increasing breakdown stress drop and decreasing thermal weakening distance
4. Breakdown work varies by several orders of magnitude between wet gouges (0.0001-4 MJ/m^2), dry gouges (0.1-5 MJ/m^2), and intact rocks (2-40 MJ/m^2)

There is an order of magnitude difference in the frictional behavior of input sediments from different subduction margins where wet, clay-present gouges show both the greatest range of breakdown work as well as the lowest values. At Cascadia, lithology plays a limited role in discriminating the structural level in which an earthquake is likely to propagate due to the lack of variability in the frictional behavior and breakdown work between mudstones and sandstones. The relatively high frictional strength and moderate breakdown work of the input sediments from the Cascadia margin suggest that it may be less susceptible to hosting very large amounts of shallow slip or dynamic overshoot, although this may be mediated by more frictionally unstable behavior of the gouge and a greater amount of elastic stored energy at shallow depth due to the higher strength of the gouges.

Acknowledgements

This research used samples and data provided by the Ocean Drilling Project (ODP) from the Gulf Coast Repository (GCR) at Texas A&M University (http://iodp.tamu.edu/curation/index.html). We thank Takahiro Suzuki for assistance with the Cascadia friction experiments and Tom Mitchell for assistance with the individual clay species friction experiments. We thank Yajing Liu for discussions on an earlier version of the manuscript. We thank Matt Ikari and Hannah Rabinowitz for insightful and constructive reviews which greatly improved the manuscript. This study was supported by a research grant from the European Consortium for Ocean Research Drilling (ECORD) and a graduate student research grant from the Geological Society of America (GSA). J.K. acknowledges support from NSERC Discovery award RGPIN-2016-04677, T.H. acknowledges support from JSPS KAKENHI Grant JP19H02006, and D.F. acknowledges support from NERC grant NE/P002943/1.

References

Abercrombie, R.E., Rice, J.R., 2005. Can observations of earthquake scaling constrain slip weakening? Geophys. J. Int. 162, 406-424. https://doi.org/10.1111/j.1365-246X.2005.02579.x.

Aretusini, S., Spagnuolo, E., Dalconi, M.C., Di Toro, G., Rutter, E.H., 2019. Water availability and deformation processes in smectite-rich gouges during seismic slip. J. Geophys. Res. Solid Earth 124, 10,855-810,876. https://doi.org/10.1029/2019JB018229.

Bletery, Q., Sladen, A., Jiang, J., Simons, M., 2016. A Bayesian source model for the 2004 great Sumatra-Andaman earthquake. J. Geophys. Res. Solid Earth 121, 5116-5135. https://doi.org/10.1002/2016JB012911.

Carson, B., Westbrook, G.K., Musgrave, R.J., Suess, E., 1995. Proceedings of the Ocean Drilling Program, Scientific Results, Vol.146 (Part 1). Ocean Drilling Program, College Station, TX.

Chester, F.M., Rowe, C., Ujiie, K., Kirkpatrick, J., Regalla, C., Remitti, F., Moore, J.C., Toy, V., Wolfson-Schwehr, M., Bose, S., Kameda, J., Mori, J.J., Brodsky, E.E., Eguchi, N., Toczko, S., Expedition 343 and 343T Scientists, 2013. Structure and composition of the plate-boundary slip zone for the 2011 Tohoku-Oki earthquake. Science 342, 1208-1211. https://doi.org/10.1126/science.1243719.

Cocco, M., Bizzarri, A., 2002. On the slip-weakening behavior of rate- and state dependent constitutive laws. Geophys. Res. Lett. 29, 1516. https://doi.org/10.1029/2001GL013999.

Cubas, N., Souloumiac, P., Singh, S.C., 2016. Relationship link between landward vergence in accretionary prisms and tsunami generation. Geology 44, 787-790. https://doi.org/10.1130/G38019.1.

Di Toro, G., Han, R., Hirose, T., De Paola, N., Nielsen, S., Mizoguchi, K., Ferri, F., Cocco, M., Shimamoto, T., 2011. Fault lubrication during earthquakes. Nature 471, 494-498. https://doi.org/10.1038/nature09838.

Faulkner, D.R., Mitchell, T.M., Behnsen, J., Hirose, T., Shimamoto, T., 2011. Stuck in the mud? Earthquake nucleation and propagation through accretionary forearcs. Geophys. Res. Lett. 38, 1-5. http://doi.wiley.com/10.1029/2011GL048552.

Fisher, A., Davis, E.E., Escutia, C., 2000. Proceedings of the Ocean Drilling Program, Scientific Results, Vol.168. Ocean Drilling Program, College Station, TX.

French, M.E., Kitajima, H., Chester, J.S., Chester, F.M., Hirose, T., 2014. Displacement and dynamic weakening processes in smectite-rich gouge from the Central Deforming Zone of the San Andreas Fault. J. Geophys. Res. Solid Earth 119, 1777-1802. https://doi.org/10.1002/2013JB010757.

Goldfinger, C., Nelson, C.H., Morey, A.E., Johnson, J.E., Patton, J.R., Karabanov, E., Gutierrez-Pastor, J., Eriksson, A., Gracia, E., Dunhill, G., Enkin, R., Dallimore, A., Vallier, T., 2012. Turbidite Event History - Methods and Implications for Holocene Paleoseismicity of the Cascadia Subduction Zone. U.S. Geological Survey, p. 170.

Han, S., Bangs, N.L., Carbotte, S.M., Saffer, D.M., Gibson, J.C., 2017. Links between sediment consolidation and Cascadia megathrust slip behaviour. Nat. Geosci. 10, 954-959. https://doi.org/10.1038/s41561-017-0007-2.

Hirose, T., Shimamoto, T., 2005. Growth of molten zone as a mechanism of slip weakening of simulated faults in gabbro during frictional melting. J. Geophys. Res. Solid Earth 110, B05202. https://doi.org/10.1029/2004JB003207.

Ida, Y., 1972. Cohesive force across the tip of a longitudinal-shear crack and Griffith's specific surface energy. J. Geophys. Res. 77, 3796-3805. https://doi.org/10.1029/JB077i020p03796.

Ikari, M., Kopf, A.J., 2017. Seismic potential of weak, near-surface faults revealed at plate tectonic slip rates. Sci. Adv. 3, e1701269. https://doi.org/10.1126/sciadv.1701269.

Ikari, M., Kopf, A.J., Hüpers, A., Vogt, C., 2018. Lithologic control of frictional strength variations in subduction zone sediment inputs. Geosphere 12, 604-625. https://doi.org/10.1130/GES01546.1.

Ikari, M.J., Saffer, D.M., Marone, C., 2009. Frictional and hydrologic properties of clay-rich fault gouge. J. Geophys. Res. Solid Earth 114, B05409. https://doi.org/10.1029/2008JB006089.

Kanamori, H., 1972. Mechanism of tsunami earthquakes. Phys. Earth Planet. Inter. 6, 346-359. https://doi.org/10.1016/0031-9201(72)90058-1.

Kirkpatrick, J.D., Rowe, C.D., Ujiie, K., Moore, J.C., Regalla, C., Remitti, F., Toy, V., Wolfson-Schwehr, M., Kameda, J., Bose, S., Chester, F.M., 2015. Structure and lithology of the Japan Trench subduction plate boundary fault. Tectonics 34, 53-69. https://doi.org/10.1002/2014TC003695.

Kitajima, H., Chester, J.S., Chester, F., Shimamoto, T., 2010. High‐speed friction of disaggregated ultracataclasite in rotary shear: Characterization of frictional heating, mechanical behavior, and microstructure evolution. J. Geophys. Res. 115, B08408. https://doi.org/10.1029/2009JB007038.

Lay, T., 2018. A review of the rupture characteristics of the 2011 Tohoku-oki Mw 9.1 earthquake. Tectonophysics 733, 4-36. https://doi.org/10.1016/j.tecto.2017.09.022.

Li, S., Wang, K., Wang, Y., Jiang, Y., Dosso, S.E., 2018. Geodetically inferred locking state of the Cascadia megathrust based on a viscoelastic earth model. J. Geophys. Res. Solid Earth 123, 8056-8072. https://doi.org/10.1029/2018JB015620.

Ma, S., 2012. A self-consistent mechanism for slow dynamic deformation and tsunami generation for earthquakes in the shallow subduction zone. Geophys. Res. Lett. 39, L11310. https://doi.org/10.1029/2012GL051854.

McGuire, J.J., Collins, J.A., Davis, E., Becker, K., Heesemann, M., 2018. A lack of dynamic triggering of slow slip and tremor indicates that the shallow Cascadia megathrust offshore Vancouver Island is likely locked. Geophys. Res. Lett. 45, 1-9. https://doi.org/10.1029/2018GL079519.

Mizoguchi, K., Hirose, T., Shimamoto, T., Fukuyama, E., 2007. Reconstruction of seismic faulting by high-velocity friction experiments: An example of the 1995 Kobe earthquake. Geophys. Res. Lett. 34, L01308. https://doi.org/10.1029/2006GL027931.

Moore, J.C., Plank, T.A., Chester, F.M., Polissar, P.J., Savage, H.M., 2015. Sediment provenance and controls on slip propagation: Lessons learned from the 2011 Tohoku and other great earthquakes of the subducting northwest Pacific plate. Geosphere 11, 533-541. https://doi.org/10.1130/GES01099.1.

Nielsen, S., Spagnuolo, E., Smith, S.A.F., Violay, M., Di Toro, G., Bistacchi, A., 2016. Scaling in natural and laboratory earthquakes. Geophys. Res. Lett. 43, 1504-1510. https://doi.org/10.1002/2015GL067490.

Noda, H., Dunham, E.M., Rice, J.R., 2009. Earthquake ruptures with thermal weakening and the operation of major faults at low overall stress levels. J. Geophys. Res. 114, B07302. https://doi.org/10.1029/2008JB006143.

Obana, K., Scherwath, M., Yamamoto, Y., Kodaira, S., Wang, K., Spence, G., Riedel, M., Kao, H., 2015. Earthquake activity in northern Cascadia subduction zone off Vancouver Island revealed by ocean-bottom seismograph observations. Bull. Seismol. Soc. Am. 105, 489-495. https://doi.org/10.1785/0120140095.

Oleskevich, D.A., Hyndman, R.D., Wang, K., 1999. The updip and downdip limits to great subduction earthquakes: Thermal and structural models of Cascadia, south Alaska, SW Japan, and Chile. J. Geophys. Res. Solid Earth 104, 14965-14991. https://doi.org/10.1029/1999JB900060.

Palmer, A.C., Rice, J.R., 1973. The growth of slip surfaces in the progressive failure of over-consolidated clay. Proc. Roy. Soc. Lond. A. 332, 527-548. https://doi.org/10.1098/rspa.1973.0040.

Rabinowitz, H.S., Savage, H.M., Polissar, P.J., Rowe, C.D., Kirkpatrick, J.D., 2020. Earthquake slip surfaces identified by biomarker thermal maturity within the 2011 Tohoku-Oki earthquake fault zone. Nat. Comm. 11, 1-9. https://doi.org/10.1038/s41467-020-14447-1.

Reches, Z., Lockner, D.A., 2010. Fault weakening and earthquake instability by powder lubrication. Nature 467, 452-455. https://doi.org/10.1038/nature09348.

Rice, J.R., 2006. Heating and weakening of faults during earthquake slip. J. Geophys. Res. Solid Earth 111, B05311. https://doi.org/10.1029/2005JB004006.

Satake, K., Wang, K., Atwater, B.F., 2003. Fault slip and seismic moment of the 1700 Cascadia earthquake inferred from Japanese tsunami descriptions. J. Geophys. Res. Solid Earth 108, 2535. https://doi.org/10.1029/2003JB002521.

Savage, H.M., Rabinowitz, H.S., Spagnuolo, E., Aretusini, S., Polissar, P.J., Di Toro, G., 2018. Biomarker thermal maturity experiments at earthquake slip rates. Earth Planet. Sci. Lett. 502, 253-261. https://doi.org/10.1016/j.epsl.2018.08.038.

Sawai, M., Hirose, T., Kameda, J., 2014. Frictional properties of incoming pelagic sediments at the Japan Trench: implications for large slip at a shallow plate boundary during the 2011 Tohoku earthquake. Earth Planets Space 66, 65. https://doi.org/10.1186/1880-5981-66-65.

Selvadurai, P.A., 2019. Laboratory insight into seismic estimates of energy partitioning during dynamic rupture: An observable scaling breakdown. J. Geophys. Res. Solid Earth 124, 1-30. https://doi.org/10.1029/2018JB017194.

Sone, H., Shimamoto, T., 2009. Frictional resistance of faults during accelerating and decelerating earthquake slip. Nat. Geosci. 2, 705-708. https://doi.org/10.1038/ngeo637.

Tanikawa, W., Mukoyoshi, H., Tadai, O., 2012. Experimental investigation of the influence of slip velocity and temperature on permeability during and after high-velocity fault slip. J. Struct. Geol. 38, 90-101. https://doi.org/10.1016/j.jsg.2011.08.013.

Tinti, E., Spudich, P., Cocco, M., 2005. Earthquake fracture energy inferred from kinematic rupture models on extended faults. J. Geophys. Res. 110, B12303. https://doi.org/10.1029/2005JB003644.

Tsutsumi, A., Shimamoto, T., 1997. High-velocity frictional properties of gabbro. Geophys. Res. Lett. 24, 699-702. https://doi.org/10.1029/97GL00503.

Ujiie, K., Tanaka, H., Saito, T., Tsutsumi, A., Mori, J.J., Toczko, S., Expedition 343 and 343T Scientists, 2013. Low coseismic shear stress on the Tohoku-Oki megathrust determined from laboratory experiments. Science 342, 1211-1214. https://doi.org/10.1126/science.1243485.

Ujiie, K., Tsutsumi, A., 2010. High‐velocity frictional properties of clay‐rich fault gouge in a megasplay fault zone, Nankai subduction zone. Geophys. Res. Lett. 37, L24310. https://doi.org/10.1029/2010GL046002.

Venkataraman, A., Kanamori, H., 2004. Observational constraints on the fracture energy of subduction zone earthquakes. J. Geophys. Res. Solid Earth 109, B05302. https://doi.org/10.1029/2003JB002549.

Viesca, R.C., Garagash, D.I., 2015. Ubiquitous weakening of faults due to thermal pressurization. Nat. Geosci. 8, 875-879. https://doi.org/10.1038/ngeo2554.

Vrolijk, P., 1990. On the mechanical role of smectite in subduction zones. Geology 18, 703-707. https://doi.org/10.1130/0091-7613(1990)018<0703:OTMROS>2.3.CO;2.

Wang, K., Hu, Y., He, J., 2012. Deformation cycles of subduction earthquakes in a viscoelastic Earth. Nature 484, 327-332. https://doi.org/10.1038/nature11032.

Yao, L., Ma, S., Platt, J.D., Niemeijer, A., Shimamoto, T., 2016. The crucial role of temperature in high-velocity weakening of faults: Experiments on gouge using host blocks with different thermal conductivities. Geology 44, 63-66. https://doi.org/10.1130/G37310.1.

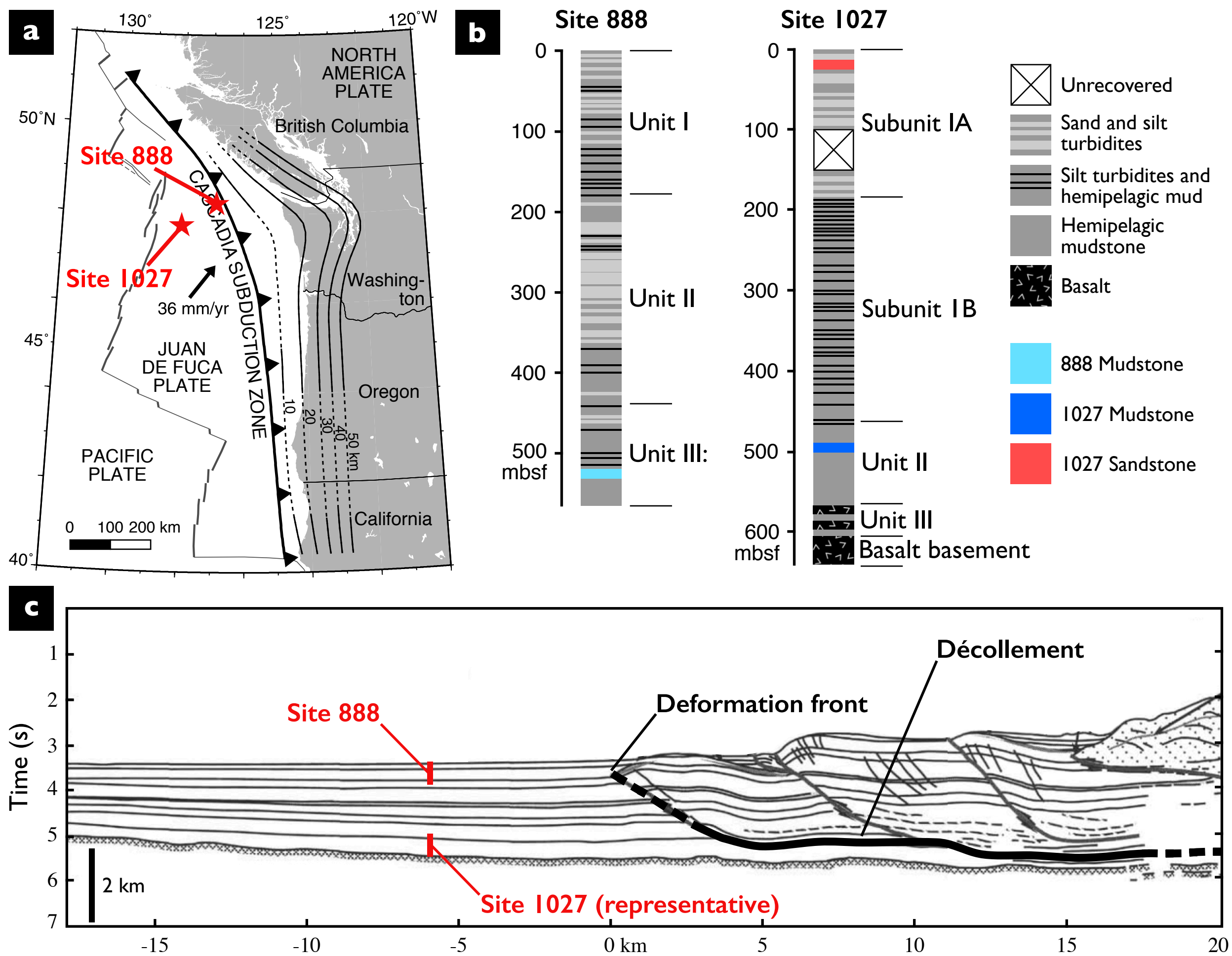

Fig. 1. Location and stratigraphy of ODP sites. **(a)** Locations of ODP sites (red stars) relative to the Cascadia subduction zone, note the sites are in a transect near parallel to the plate convergence direction (adapted from Satake et al. (2003)). **(b)** Schematic stratigraphy at ODP sites with units as defined in expedition reports (adapted from Carson et al. (1995) and Fisher et al. (2000)). Core samples selected for experiments are highlighted with colored bars. Core samples include one sample of a sand turbidite (red bar) and two samples of hemipelagic mudstones (light blue and dark blue bars). **(c)** Sketch of seismic reflection data at Site 888 showing the location of the décollement, the deformation front, and the relative depth of stratigraphy in each hole (actual depth of Site 888 and representative depth of Site 1027) (adapted from Carson et al. (1995) and Fisher et al. (2000)).

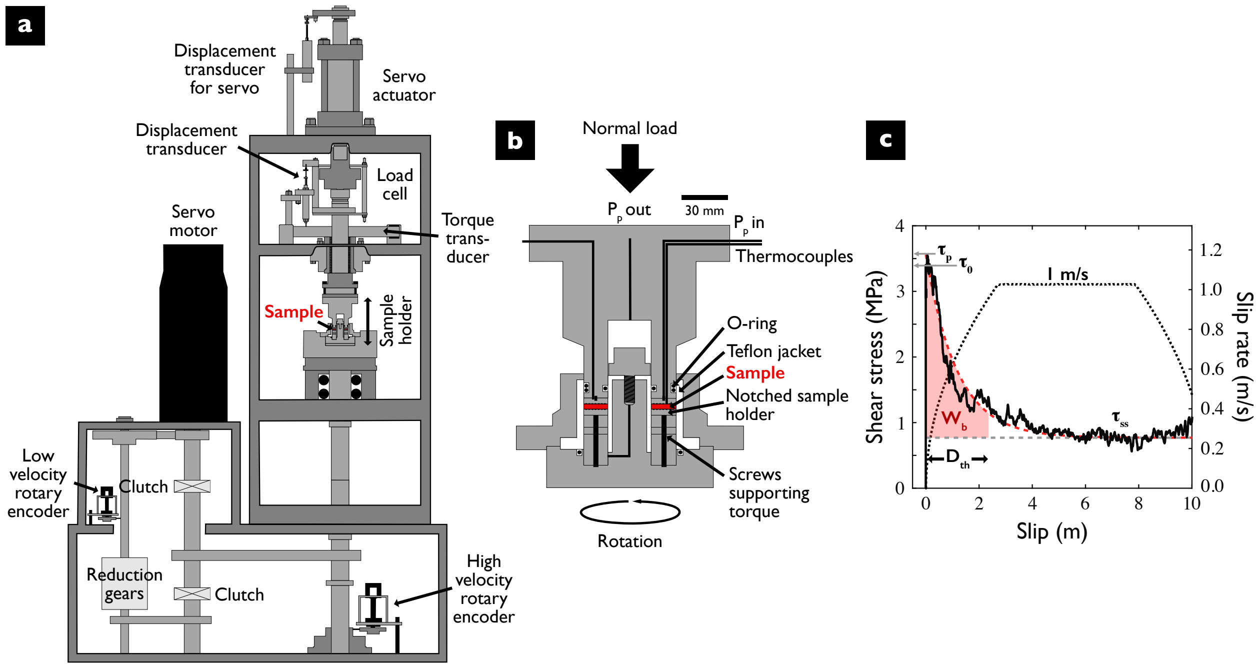

Fig. 2. Experimental apparatus. **(a)** Schematic cross-sectional diagram of low to high velocity rotary shear apparatus (PHV) at the Kochi Core Center. **(b)** Schematic cross-sectional diagram of sample assembly. **(c)** Representative mechanical data for a high velocity rotary shear experiment (black solid line), model of shear stress evolution (red dashed line), residual shear stress (grey dashed line), and slip rate (black dotted line). τ_0 is the initial shear stress before the acceleration ramp, τ_p is the peak shear stress after acceleration begins, and τ_{ss} is the steady state shear stress achieved during slip at 1 m/s. Red shaded area represents the breakdown work (W_b) estimated from the model between slip at the onset of acceleration and the thermal weakening distance (D_{th}).

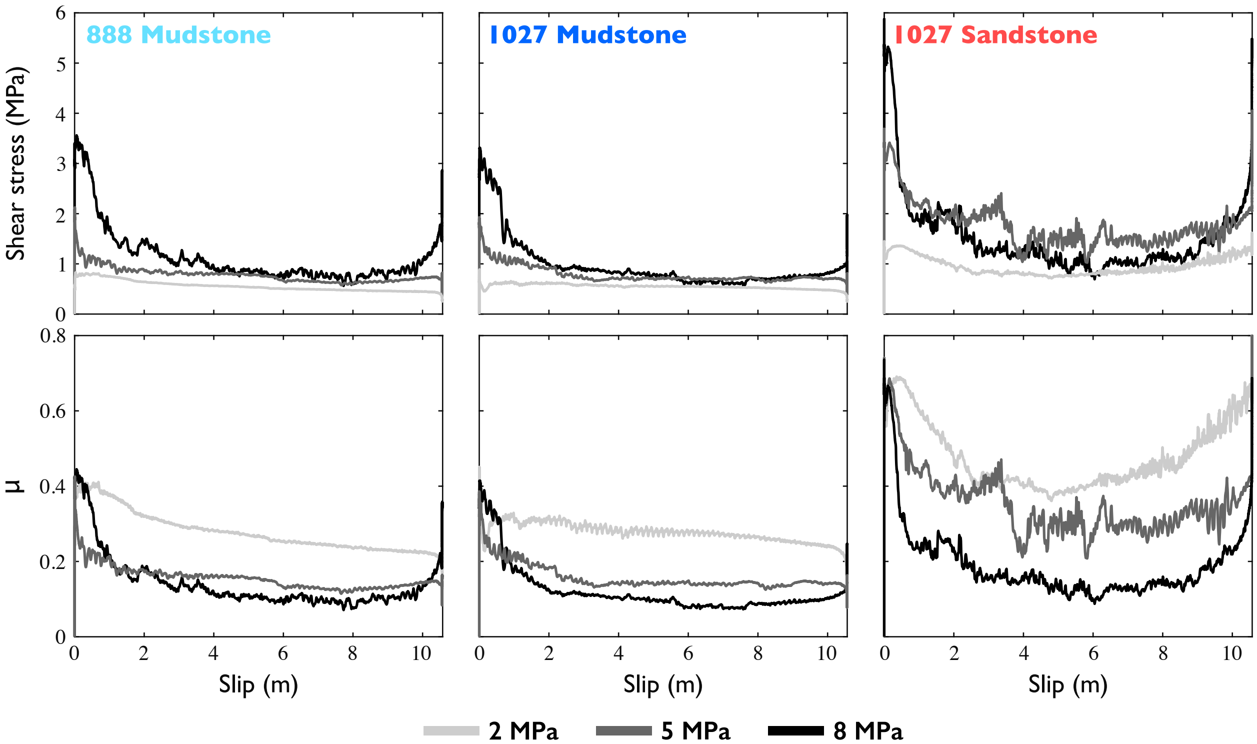

Fig. 3. Mechanical data from experiments on Cascadia core samples. **Top row:** Mechanical data plotted as shear stress versus slip showing that the steady state shear stress is consistent across normal stress conditions for each sample. **Bottom row:** Mechanical data plotted as apparent friction coefficient versus slip showing that peak friction coefficient is consistent across normal stresses while the steady state friction coefficient decreases.

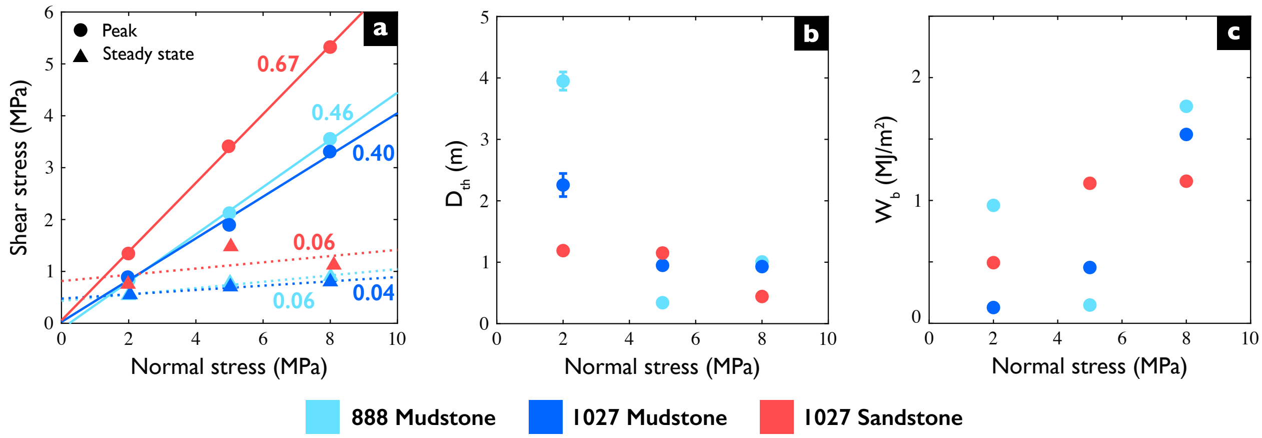

Fig. 4. Friction and fracture energy parameters from experiments on Cascadia core samples. **(a)** Shear stress scaling with normal stress for peak shear stress (circles) and steady state shear stress (triangles). Friction coefficients for each sample are defined as the linear scaling between shear stress and normal stress and are determined from the peak shear stress (solid lines) and steady state shear stress (dotted lines). **(b)** Thermal weakening distance (D_{th}) decreases with normal stress for all lithologies. Error bars from the model fit are plotted for all data points, but most do not extend beyond the circles. **(c)** Breakdown work (W_b) does not vary significantly between lithologies.

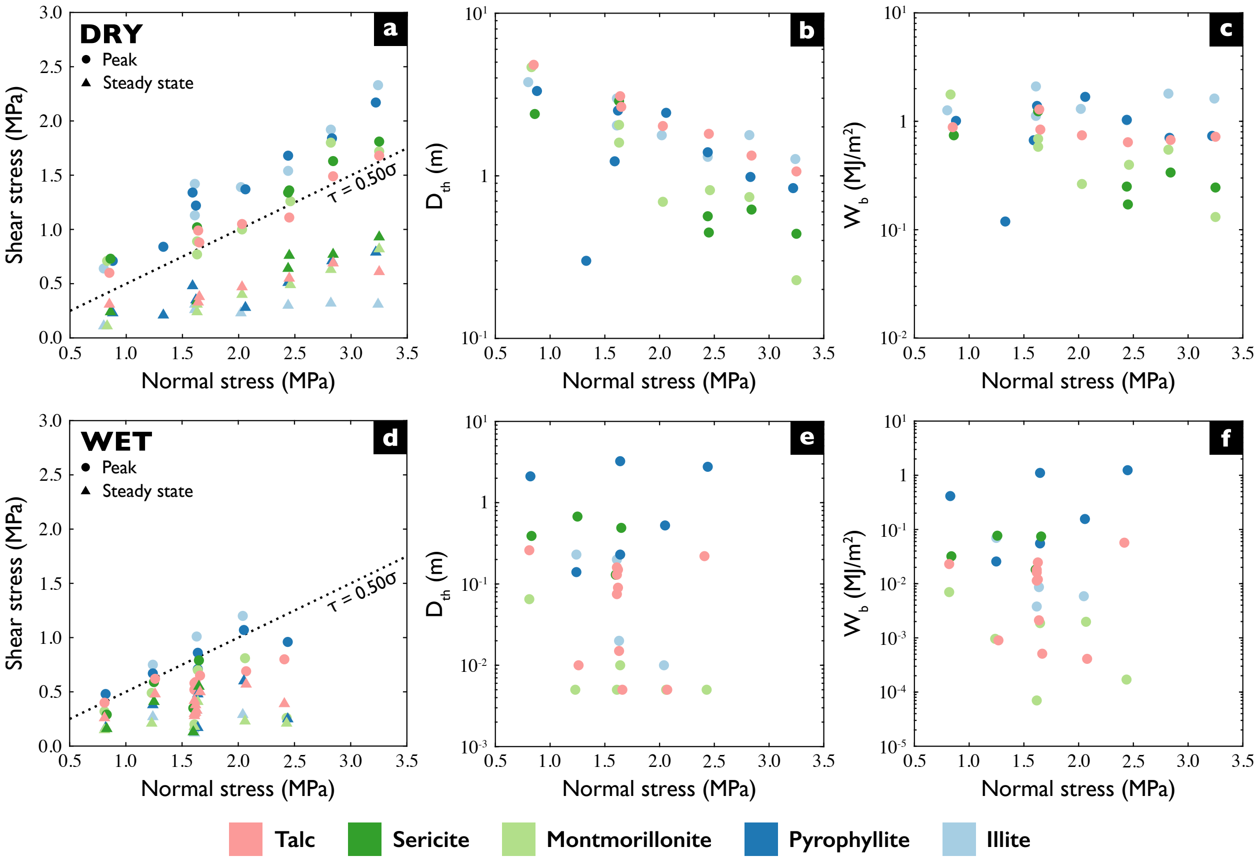

Fig. 5. Friction and fracture energy parameters from dry (a-c) and wet (d-f) experiments on individual clay species. **(a,d)** Shear stress scaling with normal stress for peak shear stress (circles) and steady state shear stress (triangles). Dashed lines show a friction coefficient of 0.50 for reference. Dry experiments have a higher peak friction coefficient than wet experiments, and steady state shear stress during dry experiments has a stronger dependence on normal stress than wet experiments. **(b,e)** Thermal weakening distance (D_{th}) decreases with normal stress for dry experiments but has no dependence on normal stress for wet experiments. **(c,f)** Breakdown work (W_b) does not vary systematically with normal stress for dry or wet experiments. Note that y-axis limits for D_{th} and W_b are different between the wet and dry conditions.

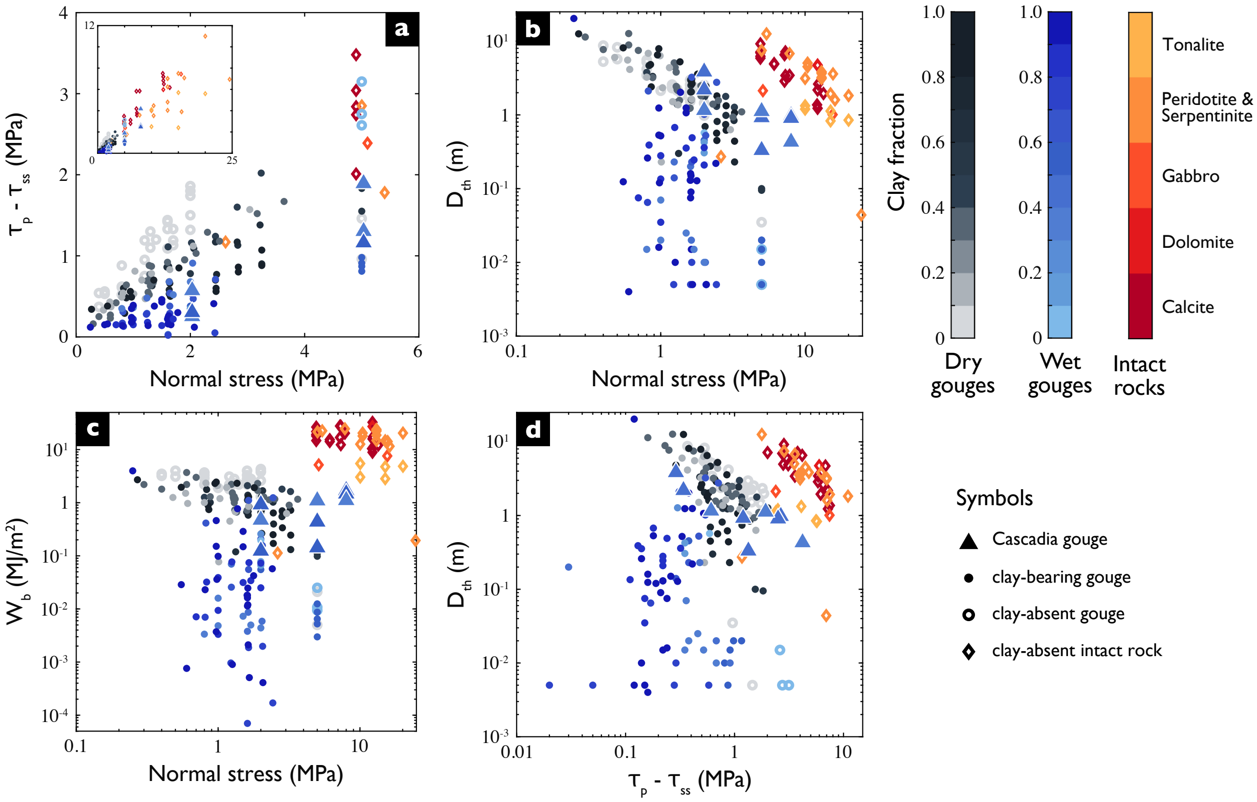

Fig. 6. Compilation of high velocity rotary shear experimental data. **(a)** Breakdown stress drop ($\tau_p - \tau_{ss}$), with inset displaying the full normal stress range, **(b)** thermal weakening distance (D_{th}), and **(c)** breakdown work (W_b) scaling with normal stress. **(d)** Thermal weakening distance (D_{th}) scaling with breakdown stress drop ($\tau_p - \tau_{ss}$).

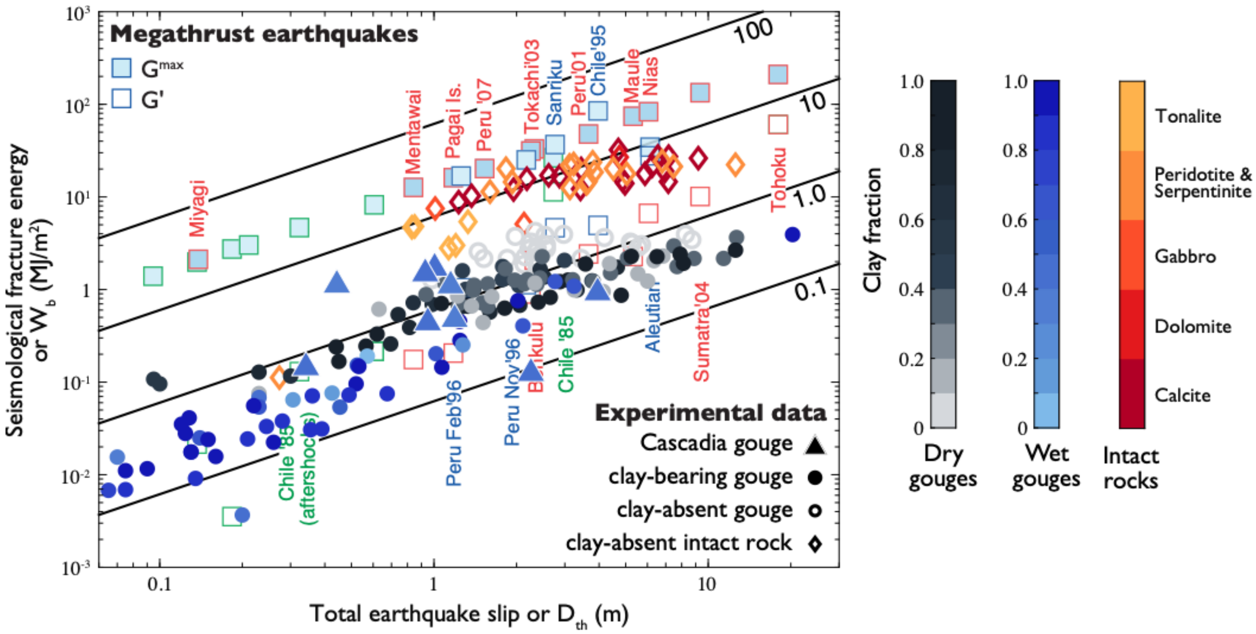

Fig. 7. Comparison between experimental and seismological estimates of fracture energy. Compilation of W_b evaluated at $\delta = D_{th}$ for high velocity rotary shear experimental data from wet gouges, dry gouges, and intact rocks imposed on the compilation of seismological estimates of fracture energy for megathrust earthquakes (Viesca and Garagash, 2015). Note that the experimental data overlies the G' fracture energy estimates for megathrust earthquakes. Black curves represent W_b calculated with Eq. 5 for constant breakdown stress drops of 0.1 to 100 MPa.

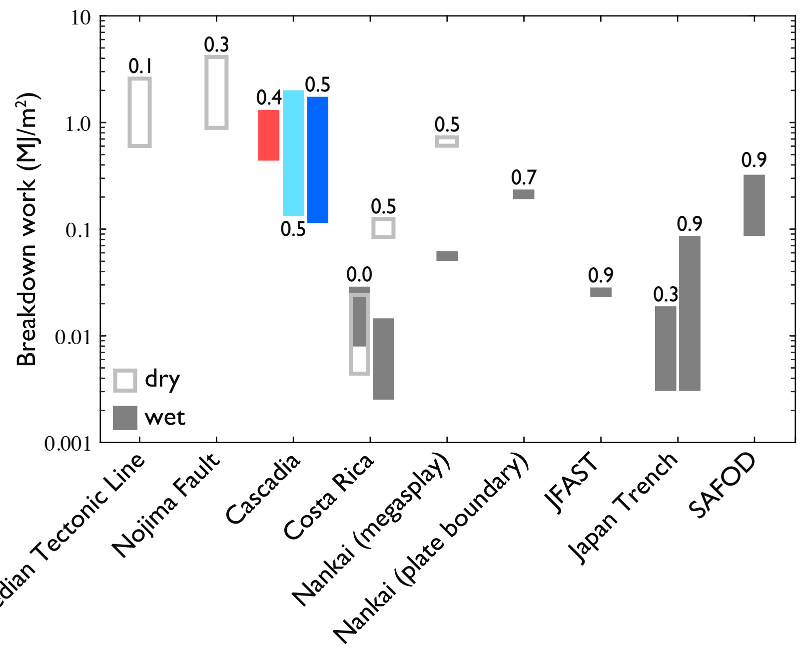

Fig. 8. Breakdown work (W_b) estimates from natural samples, including fault gouge from the Median Tectonic Line in Japan, fault gouge from the Nojima Fault in Japan, smectite-rich fault gouge from SAFOD core retrieved from the San Andreas Fault in California, sand turbidite and hemipelagic mudstones from ODP core retrieved from the input section of the Cascadia subduction zone (this study; colors are the same as in Fig. 4), megasplay and plate boundary fault gouge from IODP core retrieved from the Nankai subduction zone, smectite-rich fault gouge from IODP core retrieved from the décollement zone of the Japan Trench, pelagic sediments from DSDP core retrieved from the input section of the Japan Trench, silty clays and biogenic oozes from IODP core retrieved from the input section of the Costa Rica subduction zone. Breakdown work estimates from dry experiments (light grey) and wet experiments (dark grey) are plotted as rectangles encompassing the range of values. Numbers above or below each sample indicate the clay fraction. Data sources are listed in the supplement and Table S3.

Table 1. Experimental conditions, mechanical results, and fracture energy estimates for Cascadia samples

Run Number	Sample/ Sample name	σ_n [MPa]	τ_0 [MPa]	τ_p [MPa]	τ_{ss} [MPa]	D_{th} [m]	W_b [MJ/m^2]
PHV462	888 mudstone 888B-62X-2	2	0.49	0.83	0.54	3.949	0.960
PHV463	888 mudstone 888B-62X-2	5	1.88	2.12	0.78	0.341	0.149
PHV464	888 mudstone 888B-62X-2	8	2.92	3.56	0.90	1.005	1.766
PHV465	1027 mudstone 1027B-53X-2	2	0.61	0.89	0.55	2.257	0.129
PHV466	1027 mudstone 1027B-53X-2	5	1.49	1.90	0.70	0.949	0.455
PHV467	1027 mudstone 1027B-53X-2	8	2.74	3.31	0.80	0.929	1.537
PHV468	1027 sandstone 1027B-03H-3	2	1.27	1.36	0.75	1.189	0.494
PHV469	1027 sandstone 1027B-03H-3	5	3.34	3.41	1.48	1.150	1.140
PHV470	1027 sandstone 1027B-03H-3	8	5.30	5.33	1.12	0.442	1.157

Table 2. Power law fits to compiled data

		a_1	a_2	b	$W_b \propto \sigma_n^x$
Wet gouges	*0% clay*	0.57 ± 0.14			
	<30% clay	0.26 ± 0.06			
	>30% clay	0.19 ± 0.02			
Dry gouges	*0% clay*	0.77 ± 0.14	3.35 ± 0.40	0.90 ± 0.18	0.10
	<30% clay	0.52 ± 0.02	3.66 ± 0.67	1.00 ± 0.25	0.00
	>30% clay	0.39 ± 0.04	3.75 ± 0.47	0.98 ± 0.14	0.02
Intact rocks		0.43 ± 0.04	36.84 ± 24.94	1.03 ± 0.35	-0.03

SUPPLEMENTARY INFORMATION

Rupture to the trench? Frictional properties and fracture energy of incoming sediments at the Cascadia subduction zone

C. E. Seyler[1,*], J. D. Kirkpatrick[1], H. M. Savage[2], T. Hirose[3], and D. R. Faulkner[4]

[1] Department of Earth and Planetary Sciences, McGill University, Montréal, QC, Canada

[2] Department of Earth and Planetary Sciences, University of California, Santa Cruz, CA, USA

[3] Kochi Institute for Core Sample Research, Japan Agency for Marine-Earth Science and Technology, Kochi, Nankoku, Japan

[4] School of Environmental Sciences, University of Liverpool, Liverpool, UK

* *Corresponding author*: Caroline Seyler (caroline.seyler@mail.mcgill.ca)

S1 Supplemental methods for x-ray diffraction analyses

Sample mineralogy and dominant clay species of the selected core samples were characterized using X-ray diffraction (XRD) on whole rock powders and separated clay fractions. These results are presented in Figures S1 and S2, respectively. The core samples were ground into <90 μm powders with an alumina mortar and pestle followed by 4 minutes in the McCrone micronizing mill. Randomly oriented whole rock powders and oriented clay mounts were prepared following the methods set forth by the USGS laboratory manual for XRD (Poppe et al., 2001) to assure meaningful results. Samples were analyzed in a Rigaku SmartLab® high resolution X-ray diffractometer with Cu$K\alpha$ radiation at 40 kV and 30 mA with a 0.5° divergence slit at a continuous scan rate of 1°2θ per minute. Oriented clay mounts were analyzed untreated, expanded with ethylene glycol, and heated to 400 ˚C for clay mineral identification. Spectra collected for the whole rock powders were analyzed with Rigaku PDXL software for phase identification and composition was determined from Rietveld refinement. The uncertainty of the percentages is on the order of 5%.

S2 Supplemental methods for the high velocity friction experimental procedure

Cascadia core sample experiments were conducted in the low to high velocity rotary shear apparatus (“PHV”) at Kochi/JAMSTEC (Tanikawa et al., 2012). The machine consists of an upper stationary side from which normal load is applied and torque is measured, and a lower rotational side which is controlled by a servo motor and rotations are measured. Individual clay species experiments were conducted in the high velocity rotary shear apparatus (“HVR”) at Kochi/JAMSTEC (for more detail see Tsutsumi and Shimamoto (1997)). The machine consists of a stationary side from which normal load is applied and torque is measured, and a rotational side which has a magnetic clutch to engage the sample assembly with the motor once the desired rotation speed has been reached. The normal load is supplied by an air actuator that has the advantage that when the sample shortens during rapid slip, the normal load is maintained due to the high compressibility of air. Sample shortening was measured using a displacement transducer.

Experiments were conducted on the PHV and HVR apparatuses without gouge material, without applied normal stress, and with a gap between the sliding blocks to test the mechanical contribution of Teflon present in the sample assembly. O-rings and a Teflon jacket were components of the PHV sample assembly (Fig. 2), and a Teflon sleeve was wrapped around the gouge and adjacent sliding blocks for the HVR sample assembly. Tests conducted on the PHV apparatus used for the Cascadia core samples show negligible shear stress contributed by the O-rings and Teflon jacket (Fig. S3a). Tests conducted on the HVR apparatus used for the individual clay species shows that the shear resistance contributed by the Teflon sleeve decreases with displacement from 0.26 to 0.1 MPa (Fig. S3b). To avoid complex corrections, we have not corrected the data for the contribution of the Teflon sleeve in this study. Although the Teflon sleeve affects the mechanical data, the contribution is almost always less than the gouge and does not affect the calculated values of breakdown stress drop or breakdown work because these values are measured based on relative changes in shear stress.

For each Cascadia core sample, shear stress-normal stress pairs of the initial stress, peak stress, and steady state stress were fit to the equation $\tau = \mu\sigma + b$ to check the shear stress contribution of the O-rings and Teflon jacket (Fig. S3c). Offsets to the linear fit (b) of the initial and peak stress data for each sample is near zero, suggesting the contribution of friction between the gouge and the Teflon jacket is negligible. Offsets to the linear fit of the steady state shear stress data are non-zero, but we consider this friction to be contributed mainly by viscous shearing within the gouge layer (see Section 4). Additionally, any contribution of friction from gouge that was sheared into the space between the upper loading column and the Teflon jacket does not affect the reported values of breakdown stress drop or breakdown work in this work.

S3 Supplemental methods for the data compilation of high velocity friction experiments

High velocity experimental data and estimates of slip weakening distance and fracture energy were compiled from existing literature. This compilation focused on fault gouges, especially clay-bearing gouges, and separated the data into gouge experiments run under wet and dry conditions and intact rock experiments. The compilation included: core samples of input sediments from the Cascadia subduction zone (this study), individual clay species (this study; Faulkner et al., 2011), drill core from the Nankai megasplay (Ujiie and Tsutsumi, 2010) and plate boundary (Ujiie et al., 2013), drill core from the Japan trench (Ujiie et al., 2013), SAFOD core from the San Andreas Fault (French et al., 2014), synthetic smectite-rich gouge (Oohashi et al., 2015), drill core of input sediments from the Costa Rica margin (Vannucchi et al., 2017), drill core of input sediments from the Japan Trench (Sawai et al., 2014), talc gouge (Boutareaud et al., 2012), Nojima Fault gouge (Mizoguchi et al., 2007; Sawai et al., 2012), fault gouge from the Median Tectonic Line (Brantut et al., 2008), Longmenshan fault gouge (Togo et al., 2011), and serpentinite (Hirose and Bystricky, 2007) as well as the experiments on anhydrite gouge, dolomite gouge, gypsum gouge, Carrara marble, dolomite, gabbro, peridotite, and tonalite previously complied by Di Toro et al. (2011).

All experiments in this compilation were run either on the horizontal high velocity rotary shear machine at Kochi/JAMSTEC (“HVR”), the high velocity rotary friction apparatus at Kyoto University, the low to high velocity rotary friction apparatus (“PHV”) at Kochi/JAMSTEC, the low to high velocity rotary friction apparatus (“HDR”) at Hiroshima University, or the slow to high velocity apparatus (“SHIVA”) at the National Institute of Geophysics and Volcanology (INGV). All experiments conducted on intact rock and the majority of gouge experiments were run on the HVR apparatus. Experiments conducted on the HVR, HDR, and Kyoto apparatuses used solid cylinders of rock (sandstone or gabbro) as sample holders. Experiments conducted on the PHV apparatus and SHIVA used impermeable steel ring-shaped sample holders that have a larger diameter than the solid cylinders used on the other machines. This introduces some inconsistency in the permeability of the sample holders, thermal conductivity of the apparatus, and the slip velocity gradient. Additionally, we are unable to evaluate any effects due to differences in the acceleration ramp during experiments because acceleration is often not reported. Previous work on acceleration found that the acceleration path does affect the stress evolution. Faster acceleration rates result in more rapid weakening (i.e. shorter characteristic slip distances) and a higher peak shear stress but does not change the steady state shear stress (Chang et al., 2012; Hirose et al., 2011; Liao et al., 2014; Niemeijer et al., 2011; Sone and Shimamoto, 2009). These combined effects may cancel each other and produce minor changes in the breakdown work (Hirose et al., 2011).

Reported slip weakening distance data was converted to thermal weakening distance to estimate breakdown work. The conventional method for estimating slip weakening distance (D_c) defines a threshold for the reduction of shear stress to 5% of the breakdown stress drop ($\tau_p - \tau_{ss}$), whereas the method for estimating the thermal weakening distance (D_{th}) defines this threshold based on the e-folding distance (a reduction to ~36%). Both models use the same exponential decay curve and the same starting (τ_p) and ending (τ_{ss}) values (Fig. S5), so D_{th} can be determined from the conventionally reported data. To convert from D_c to D_{th}, the shear stress curve was modeled with reported τ_p, τ_{ss}, and D_c values according to the slip weakening model

$$\tau(\delta) = \tau_{ss} + (\tau_p - \tau_{ss})e^{\frac{\ln(0.05)\delta}{D_c}} \qquad (S1)$$

Then, the thermal weakening model (Eq. 4) was solved at $\delta = D_{th}$ to find the shear stress value

$$\tau(D_{th}) = \tau_{ss} + (\tau_p - \tau_{ss})e^{-\frac{D_{th}}{D_{th}}} \qquad (S2)$$

Next, D_{th} was determined by finding the slip along the model where $\tau = \tau(D_{th})$. Finally, breakdown work (W_b) was then estimated with the newly converted D_{th} by integrating under the model from zero to $\delta = D_{th}$ (Eq. 5).

References

Boutareaud, S., Hirose, T., Andréani, M., Pec, M., Calugaru, D.-G., Boullier, A.M., Doan, M.L., 2012. On the role of phyllosilicates on fault lubrication: Insight from micro- and nanostructural investigations on talc friction experiments. J. Geophys. Res. 117, B08408. https://doi.org/10.1029/2011JB009006.

Brantut, N., Schubnel, A., Rouzaud, J.-N., Brunet, F., Shimamoto, T., 2008. High-velocity frictional properties of a clay-bearing fault gouge and implications for earthquake mechanics. J. Geophys. Res. 113, B10401. https://doi.org/10.1029/2007JB005551.

Chang, J.C., Lockner, D.A., Reches, Z., 2012. Rapid acceleration leads to rapid weakening in earthquake-like laboratory experiments. Science 338, 101-105. https://doi.org/10.1126/science.1221195.

Di Toro, G., Han, R., Hirose, T., De Paola, N., Nielsen, S., Mizoguchi, K., Ferri, F., Cocco, M., Shimamoto, T., 2011. Fault lubrication during earthquakes. Nature 471, 494-498. https://doi.org/10.1038/nature09838.

Faulkner, D.R., Mitchell, T.M., Behnsen, J., Hirose, T., Shimamoto, T., 2011. Stuck in the mud? Earthquake nucleation and propagation through accretionary forearcs. Geophys. Res. Lett. 38, 1-5. https://doi.org/10.1029/2011GL048552.

French, M.E., Kitajima, H., Chester, J.S., Chester, F.M., Hirose, T., 2014. Displacement and dynamic weakening processes in smectite-rich gouge from the Central Deforming Zone of the San Andreas Fault. J. Geophys. Res. Solid Earth 119, 1777-1802. https://doi.org/10.1002/2013JB010757.

Hirose, T., Bystricky, M., 2007. Extreme dynamic weakening of faults during dehydration by coseismic shear heating. Geophys. Res. Lett. 34, L14311. https://doi.org/10.1029/2007GL030049.

Hirose, T., Mukoyoshi, H., Tanikawa, W., Lin, W., Tadai, O., Noda, H., 2011. Frictional response of accreted sediments to seismic slip propagation along subduction plate boundary faults, Abstract T21B-2359 presented at 2011 Fall Meeting, AGU, San Francisco, California.

Liao, Z., Chang, J.C., Reches, Z., 2014. Fault strength evolution during high velocity friction experiments with slip-pulse and constant-velocity loading. Earth Planet. Sci. Lett. 406, 93-101. https://doi.org/10.1016/j.epsl.2014.09.010.

Mizoguchi, K., Hirose, T., Shimamoto, T., Fukuyama, E., 2007. Reconstruction of seismic faulting by high-velocity friction experiments: An example of the 1995 Kobe earthquake. Geophys. Res. Lett. 34, L01308. https://doi.org/10.1029/2006GL027931.

Niemeijer, A., Di Toro, G., Nielsen, S., Di Felice, F., 2011. Frictional melting of gabbro under extreme experimental conditions of normal stress, acceleration, and sliding velocity. J. Geophys. Res. 116, B07404. https://doi.org/10.1029/2010JB008181.

Oohashi, K., Hirose, T., Takahashi, M., Tanikawa, W., 2015. Dynamic weakening of smectite-bearing faults at intermediate velocities: Implications for subduction zone earthquakes. J. Geophys. Res. Solid Earth 120, 1572-1586. https://doi.org/10.1002/2015JB011881.

Poppe, L.J., Paskevich, V.F., Hathaway, J.C., Blackwood, D.S., 2001. A laboratory manual for X-ray powder diffraction. U.S. Geological Survey.

Sawai, M., Hirose, T., Kameda, J., 2014. Frictional properties of incoming pelagic sediments at the Japan Trench: implications for large slip at a shallow plate boundary during the 2011 Tohoku earthquake. Earth Planets Space 66, 65. https://doi.org/10.1186/1880-5981-66-65.

Sawai, M., Shimamoto, T., Togo, T., 2012. Reduction in BET surface area of Nojima fault gouge with seismic slip and its implication for the fracture energy of earthquakes. J. Struct. Geol. 38, 117-138. https://doi.org/10.1016/j.jsg.2012.01.002.

Sone, H., Shimamoto, T., 2009. Frictional resistance of faults during accelerating and decelerating earthquake slip. Nat. Geosci. 2, 705-708. https://doi.org/10.1038/ngeo637.

Tanikawa, W., Mukoyoshi, H., Tadai, O., 2012. Experimental investigation of the influence of slip velocity and temperature on permeability during and after high-velocity fault slip. J. Struct. Geol. 38, 90-101. https://doi.org/10.1016/j.jsg.2011.08.013.

Togo, T., Shimamoto, T., Ma, S., Hirose, T., 2011. High-velocity frictional behavior of Longmenshan fault gouge from Hongkou outcrop and its implications for dynamic weakening of fault during the 2008 Wenchuan earthquake. Earthquake Science 24, 267-281. https://doi.org/10.1007/s11589-011-0790-6.

Tsutsumi, A., Shimamoto, T., 1997. High-velocity frictional properties of gabbro. Geophys. Res. Lett. 24, 699-702. https://doi.org/10.1029/97GL00503.

Ujiie, K., Tanaka, H., Saito, T., Tsutsumi, A., Mori, J.J., Toczko, S., Expedition 343 and 343T Scientists, 2013. Low coseismic shear stress on the Tohoku-Oki megathrust determined from laboratory experiments. Science 342, 1211-1214. https://doi.org/10.1126/science.1243485.

Ujiie, K., Tsutsumi, A., 2010. High-velocity frictional properties of clay-rich fault gouge in a megasplay fault zone, Nankai subduction zone. Geophys. Res. Lett. 37, L24310. https://doi.org/10.1029/2010GL046002.

Vannucchi, P., Spagnuolo, E., Aretusini, S., Di Toro, G., Ujiie, K., Tsutsumi, A., Nielsen, S., 2017. Past seismic slip-to-the-trench recorded in Central America megathrust. Nat. Geosci. 10, 935-940. https://doi.org/10.1038/s41561-017-0013-4.

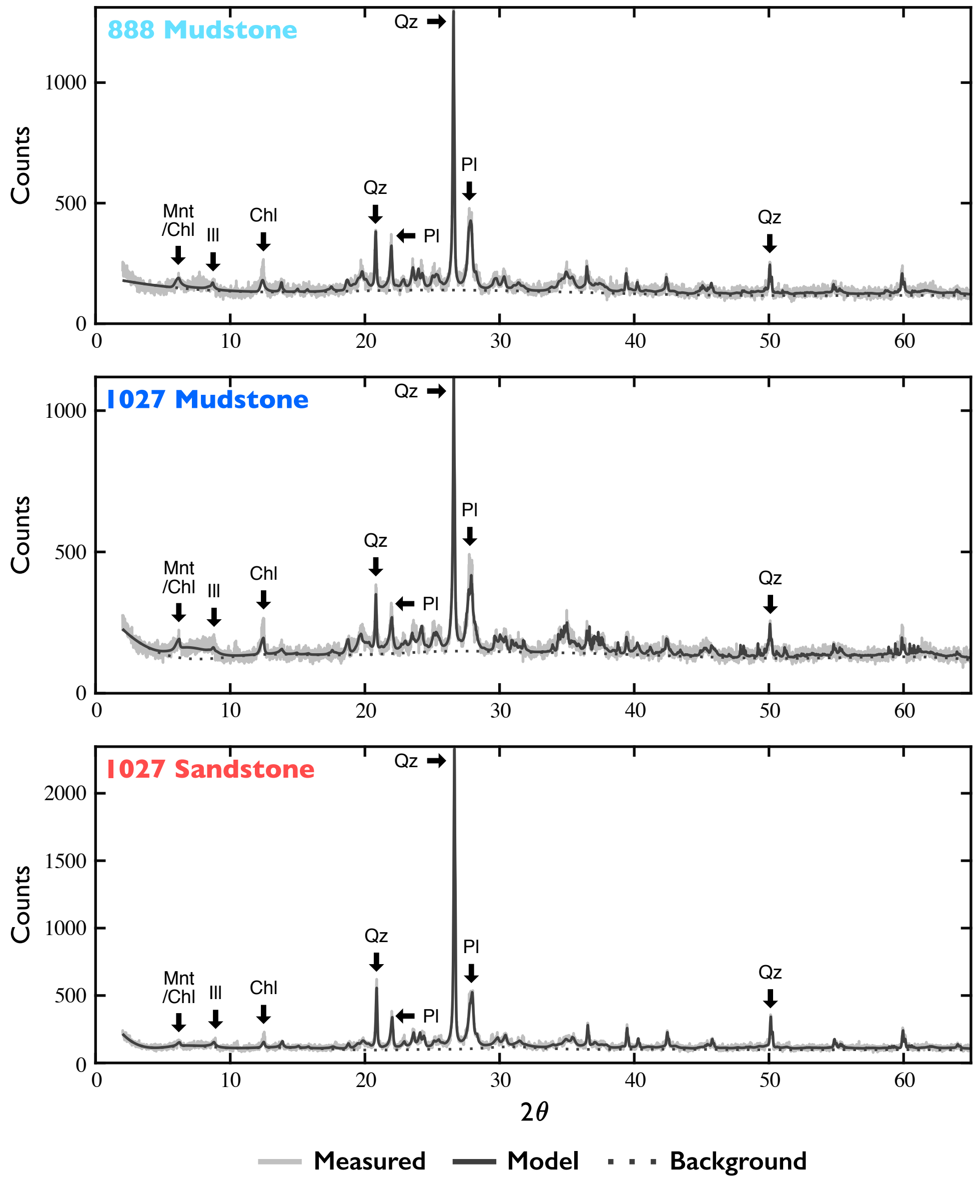

Fig. S1. Composition of Cascadia core samples. X-ray diffraction (XRD) spectra from random powder mounts prepared from the whole rock showing mineralogy identified based on characteristic d-spacings at a given 2θ (indicated with arrows). Quartz (Qz), plagioclase (Pl), montmorillonite (Mnt), chlorite (Chl), and illite (Ill) were identified in all three samples.

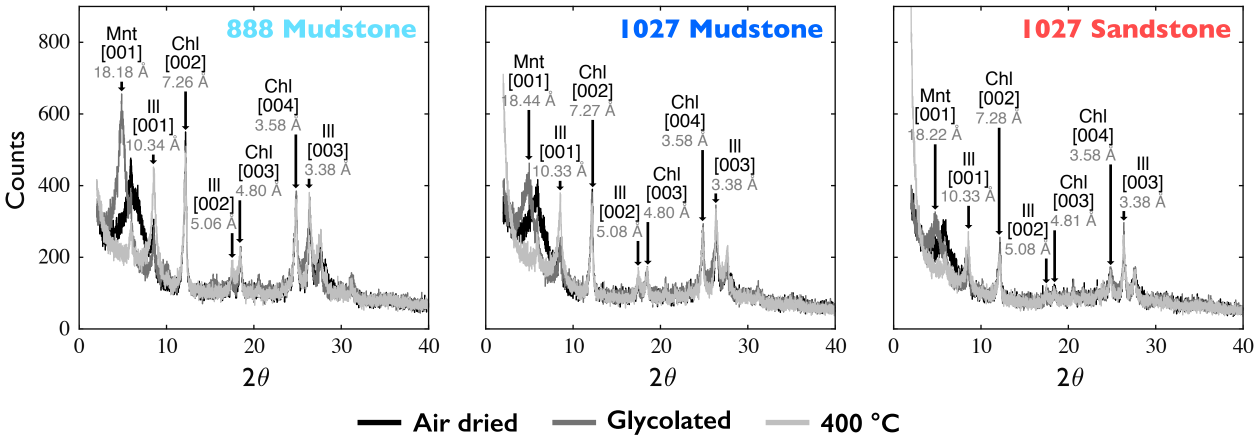

Fig. S2. Clay fraction of Cascadia core samples. X-ray diffraction (XRD) spectra from oriented mounts prepared from the clay fraction. Data was collected after samples were air dried (black line), glycolated (dark grey line), and heated to 400°C (light grey line). Clay minerals are identified based on characteristic d-spacings determined by the spacing width in ångstroms (indicated by labelled arrows). Montmorillonite (Mnt), chlorite (Chl), and illite (Ill) were identified in all three samples.

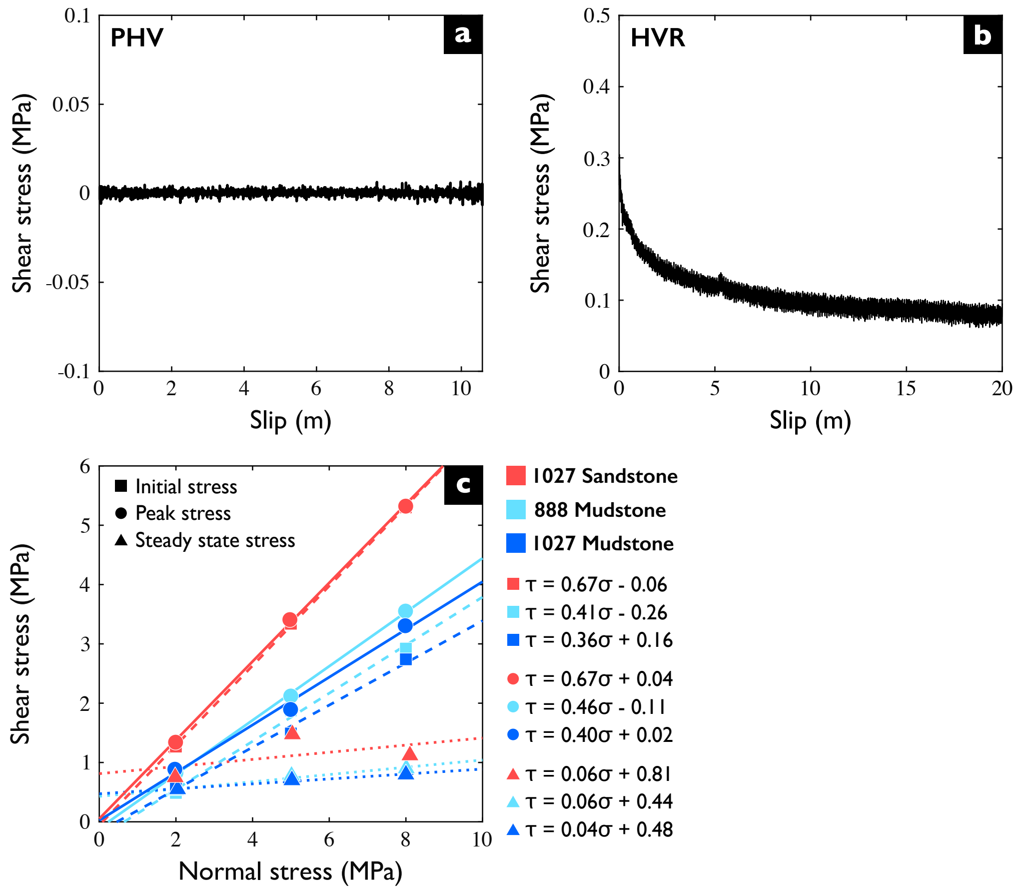

Fig. S3. Negligible contribution of Teflon to friction during experiments. Mechanical data from experiments conducted without gouge material, without applied normal stress, and with a gap between the sliding blocks to test the mechanical contribution of Teflon present in the sample assembly. **(a)** Test conducted on the low to high velocity rotary shear apparatus (PHV) used for the Cascadia core samples shows negligible shear stress contributed by the Teflon O-ring. **(b)** Test conducted with a Teflon sleeve (2 mm length) on the high velocity rotary shear apparatus (HVR) used for the individual clay species shows that the resistance contributed by the Teflon sleeve is almost always less than the gouge, so the contribution of the Teflon sleeve is negligible. **(c)** For each of the Cascadia core samples, shear stress-normal stress pairs for the initial stress (τ_0) during v_e = 500 µm/s (squares and dashed lines), peak stress (τ_p) (circles and solid lines), and steady state stress (τ_{ss}) (triangles and dotted lines) are fit with a linear equation and listed in the format $\tau = \mu\sigma + b$, where µ represents the friction coefficient.

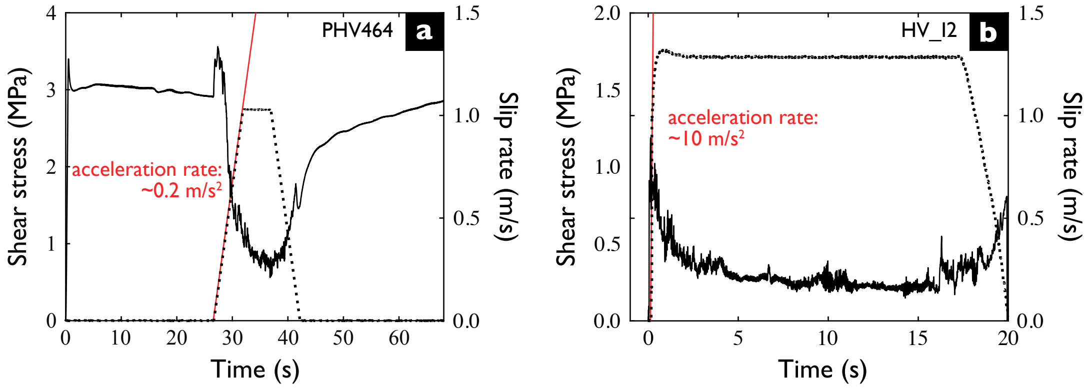

Fig. S4. Velocity and acceleration paths during experiments. **(a)** Mechanical data (solid black line) and slip rate (dotted black line) from experiment PHV464. The acceleration ramp has a rate of ~0.2 m/s^2. **(b)** Mechanical data (solid black line) and slip rate (dotted black line) from experiment HV_I2 (dry illite). The acceleration ramp has a rate of ~10 m/s^2.

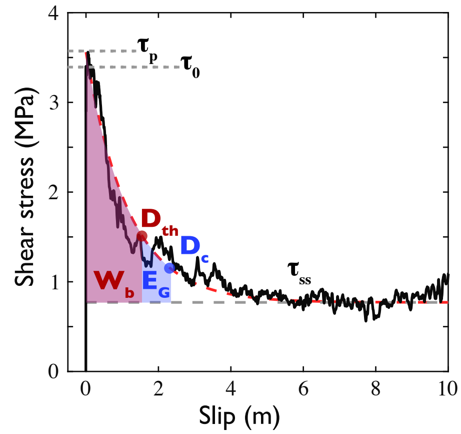

Fig. S5. Conversion of slip weakening distance (D_c) to thermal weakening distance (D_{th}). Mechanical data (black solid line), model of shear stress evolution (red dashed line), residual shear stress (grey dashed line), and slip rate (black dotted line). τ_0 is the initial shear stress before the acceleration ramp, τ_p is the peak shear stress after acceleration begins, and τ_{ss} is the steady state shear stress achieved during slip at 1 m/s. Blue shaded area represents the fracture energy (E_G) estimated from the model between slip at the onset of acceleration and D_c. Red shaded area represents the breakdown work (W_b) estimated from the model between slip at the onset of acceleration and D_{th}. Red shaded area appears purple due to the overlap with the blue shaded area. Thermal weakening distance can be determined from D_c, τ_p, and τ_{ss} using Eq. S1 and S2.

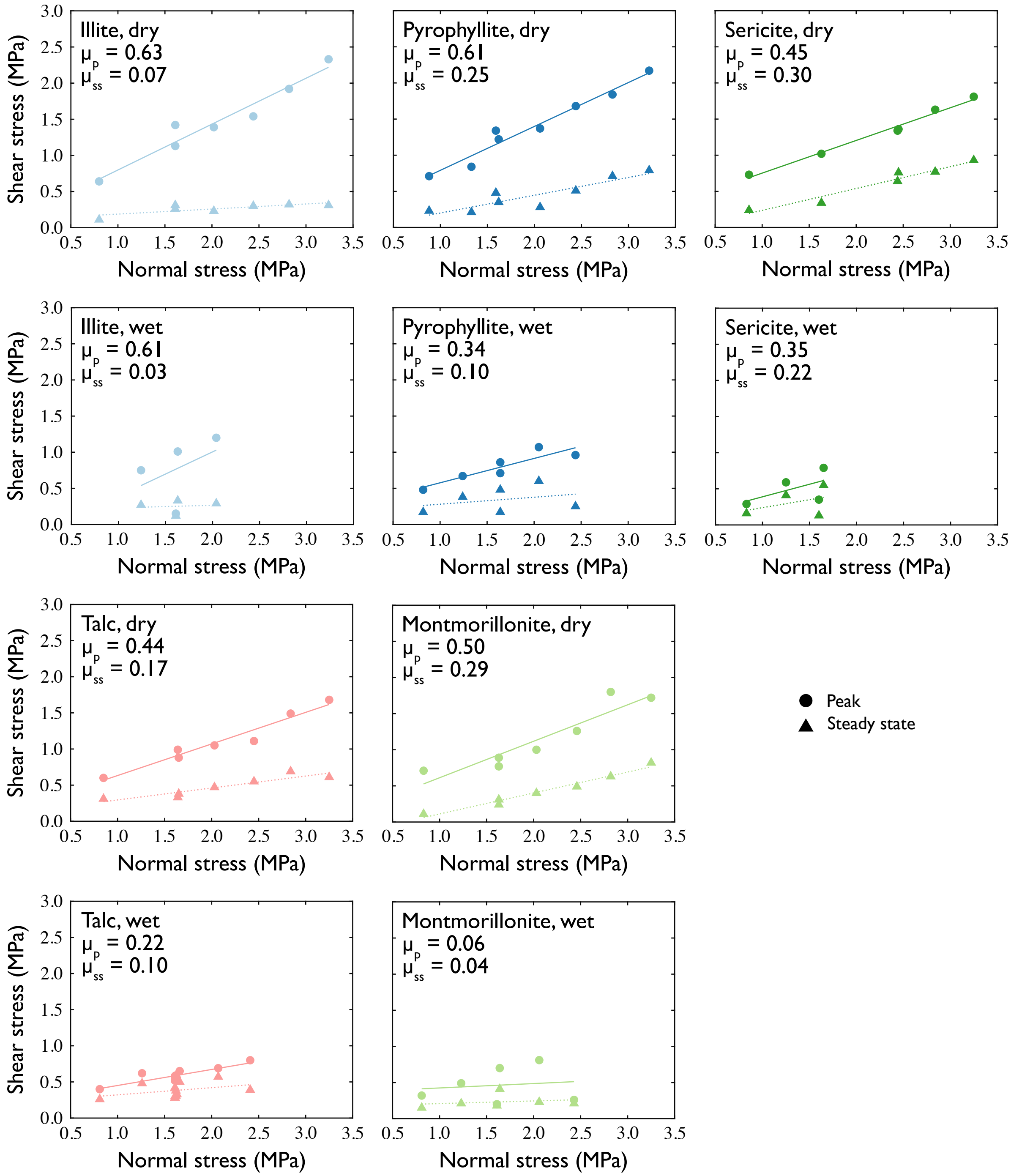

Fig. S6. Friction coefficients of individual clay species. Shear stress scaling with normal stress for peak shear stress (circles) and steady state shear stress (triangles). Friction coefficients for each sample are defined as the linear scaling between shear stress and normal stress and are determined from the peak shear stress (solid lines) and steady state shear stress (dotted lines).

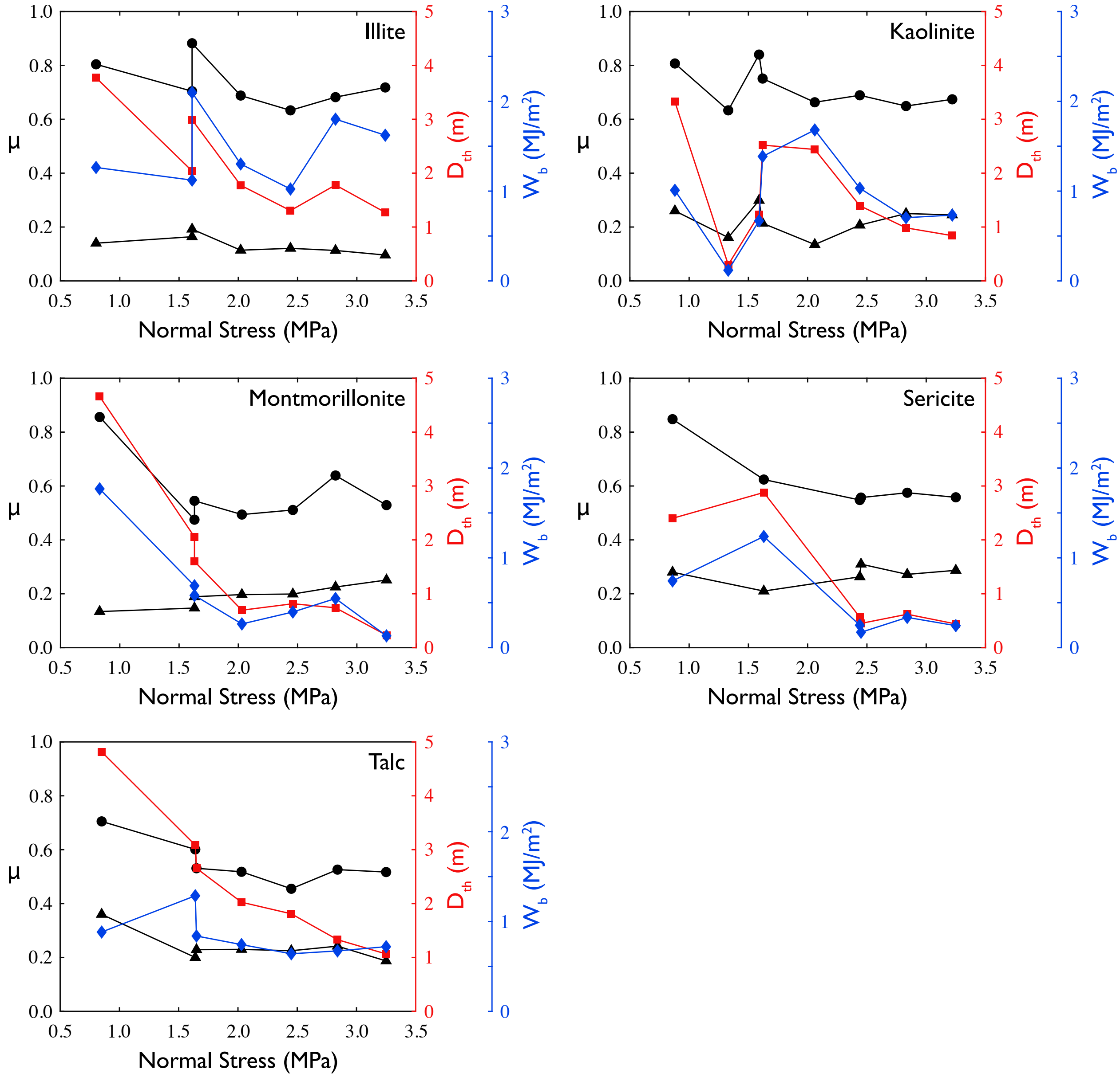

Fig. S7. Friction and fracture energy parameters from experiments conducted on individual clay species under dry conditions.

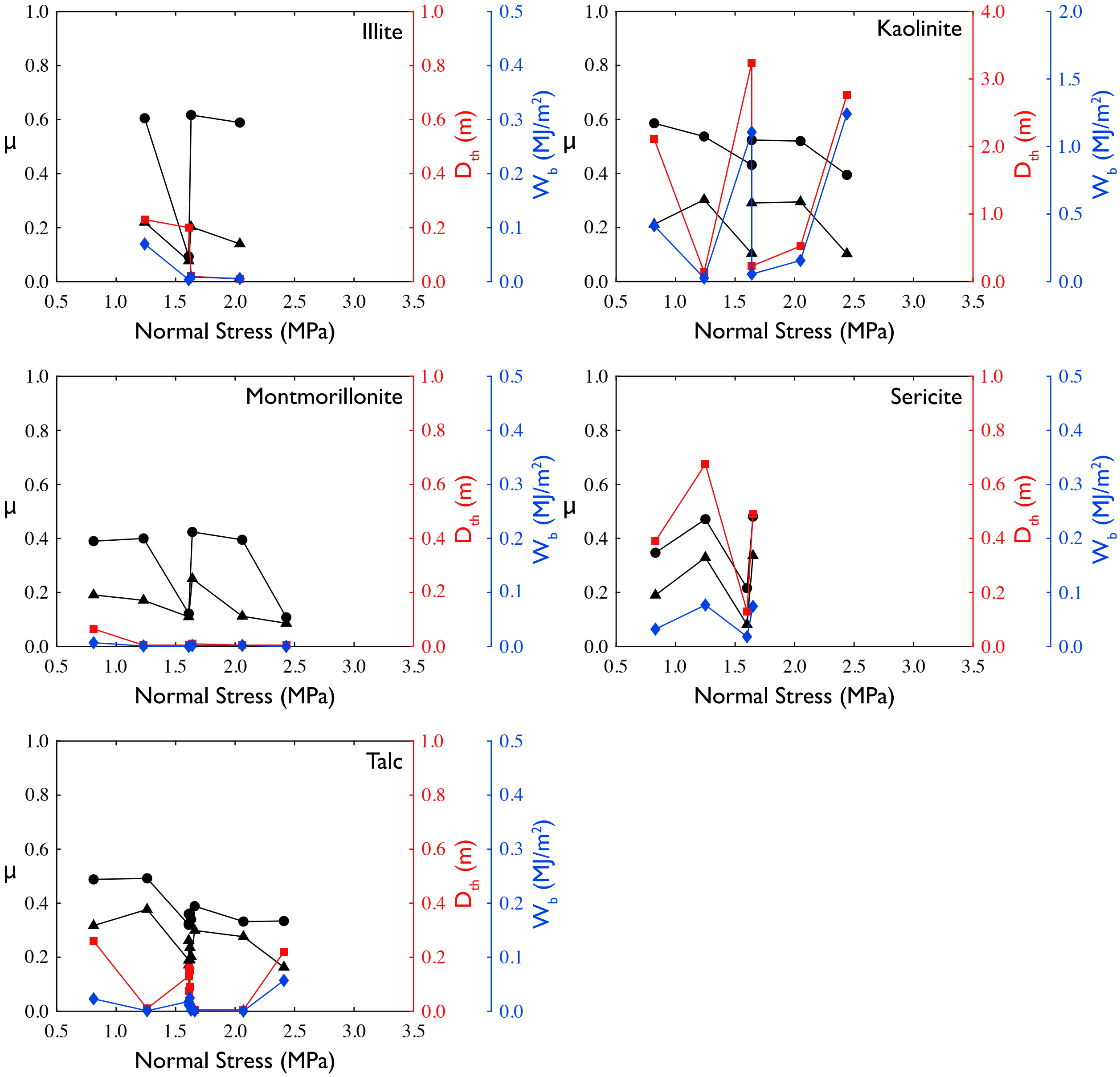

Fig. S8. Friction and fracture energy parameters from experiments conducted on individual clay species under wet conditions.

Table S1. Composition of core samples from Cascadia from XRD analysis and Rietveld refinement

Sample	Qz (%)	Fsp (%)	Clays (%)
888B-62X-2	20	35	45
1027B-03H-3	30	35	35
1027B-53X-2	20	35	45

Table S2. Composition of individual clay species samples from XRD analysis

Sample	Purity	Other components	Supplier/source
Illite	44%	Quartz 31%, calcite 24%, chlorite 1%	Peach Pig illite clay, Japan
Pyrophyllite	49%	Quartz 32%, kaolinite 14%, muscovite 5%	Nakarai Chemicals, Japan
Montmorillonite	77%	Quartz 15%, albite 8%	Na-bentonite, Yamagata Prefecture, Japan
Sericite	85%	Calcite 13%, chlorite 2%	JCSS-5101, Japan
Talc	88%	Chlorite 9%, quartz 2%, dolomite 1%	J.T. Baker, USA

Table S3. Compilation of laboratory data from high velocity rotary shear experiments